Sound radiation and non-negative intensity of a metaplate consisting of an acoustic black hole plus local resonators

Jie Deng, Oriol Guasch, Laurent Maxit, Nansha Gao

Sound radiation and non-negative intensity of a metaplate consisting of an acoustic black hole plus local resonators

Jie Deng[a,*], Oriol Guasch[b], Laurent Maxit[c], Nansha Gao[d,**]

[a]*Key Laboratory of Ocean Acoustic and Sensing, School of Marine Science and Technology, Northwestern Polytechnical University, Xian 710072, China*
[b]*GTM - Grup de Recerca en Tecnologies Mèdia, La Salle, Universitat Ramon Llull C/ Quatre Camins 30, 08022 Barcelona, Catalonia (Spain)*
[c]*INSALyon, Laboratoire Vibrations-Acoustique (LVA) 25 bis, av. Jean Capelle, F-69621 Villeurbanne Cedex, France*
[d]*Key Laboratory of Unmanned Underwater Vehicle, School of Marine Science and Technology, Northwestern Polytechnical University, Xian 710072, China*

Abstract

While acoustic black holes (ABHs) have revealed as a lightweight and efficient way to reduce structural vibrations and sound radiation, it is well-known that their range of application limits to mid-high frequencies. However, recent theoretical research has shown that by attaching periodic local resonators to an ABH plate, broadband vibration reduction can be attained, also covering the low frequency range. Such metamaterial ABH plate, hereafter referred to as the MMABH plate, could be also effective in suppressing broadband sound radiation. To that goal, we first briefly review how to compute the vibration field of the MMABH using the Gaussian expansion component mode synthesis (GECMS) method. Then we characterize the far-field acoustic radiation of the MMABH and analyze its sound power level and radiation efficiency using a discrete radiation model. The non-negative intensity (NNI) on the MMABH surface is also computed to determine which regions of the plate are responsible for the far-field, and avoid the recirculation problem associated with standard intensity calculations. It is observed that the MMABH can substantially reduce sound radiation at all frequencies thanks to the combination of several mechanisms. In the low-frequency range, the formation of bandgaps induces a low-frequency coincidence effect with air that becomes beneficial, while at mid-high frequencies supersonic bending waves entering the ABH slow down and become subsonic once passed the transonic boundary. Their radiation efficiency experiences a big drop, resulting in poor outwards radiation. Simulations of all these phenomena are presented and detailed physical background explanations are provided.

Keywords: Acoustic black holes, Metamaterials, Sound radiation, Broadband, Non-negative intensity

1. Introduction

The advent of acoustic black holes (ABHs) [1] in recent years has provided a lightweight, efficient means to reduce structural vibrations and sound radiation in the mid-high frequency range. An ABH indentation is typically achieved by diminishing the thickness to zero in a region of a given structure, following a power law profile. The flexural waves propagating inside the ABH slow down and concentrate at its center, or tip [2], where their energy can be dissipated using a thin single viscoelastic layer [3], or a constrained one [4] (among other possibilities). To date, different ABH designs have been proposed such as wedge [1, 2] and spiral [5, 6] decreasing terminations at the end of beams, and circular [7–9], rectangular [10], double compound [11, 12] or ring-shaped [13] indentations in plates. Recently, ABHs have also been designed to

*Corresponding Author: dengjie@nwpu.edu.cn
**Corresponding Author: gaonansha@nwpu.edu.cn

be embedded in circular beams [14] and cylindrical shells [15, 16]. A recent and insightful review on ABHs is provided in [17]. It is to be noted, though, that despite a large amount of theoretical and experimental literature exists on the benefits of the ABH effect for structural vibration reduction, works dealing with its influence on sound radiation are less common and rather recent.

The potential of ABHs to reduce sound radiation from plates was initially explored in [18], where experiments were performed on a plate containing an array of six ABHs, patched with small damping layers. The results showed that the sound power level (SWL) was reduced in 10-18 dB in the 1-3 kHz range, as compared to the SWL of a reference uniform plate. At the same time, computational simulations were carried out in [19] for the vibroacoustics of a plate with an embedded array of 25 ABHs. The authors reported how in addition to the vibration reduction, the radiation efficiency substantially drops once past the ABH cut-on frequency. Wavenumber analysis helped understanding the underlying physical phenomenon [20, 21]. In [22, 23], it was clearly reported how flexural supersonic waves become subsonic beyond a given frequency-dependent transonic boundary inside the ABH. Consequently, the ABH area inside the transonic boundary radiates very poorly. Experimental validation followed in [24, 25]. In addition to free-field radiation, a few more complex vibroacoustic situations have been analyzed from an experimental and numerical point of view. For instance, in [21, 26, 27] ABH plate noise radiation inside a cavity was investigated, while transmission loss between cavities separated by ABH plates were studied in [28–30].

As one could have expected, though, none of the above works reported sound radiation reduction below the ABH cut-on frequency, $f_{\mathrm{cut-on}}$. In this paper, we will refer to $f \ll f_{\mathrm{cut-on}}$, $f \sim f_{\mathrm{cut-on}}$, and $f \gg f_{\mathrm{cut-on}}$ as the low, mid, and high frequency ranges, respectively. The ABH effect essentially works for the mid-high frequency range because of size limitations. At low frequencies, the radius of the ABH must be very large to act on impinging waves, which is unfeasible from a practical point of view. Therefore, a lot of current research focuses on finding ways to complement the ABH effect to attain broadband vibration reduction in plates. For instance, nonlinear effects are being exploited for that purpose [31–35] as well as optimization techniques [36–39], which have provided promising results. Periodic distribution of ABHs on plates have proved effective too [40]. Also, the effects of non-locality to expand the range of applicability of ABHs are being explored [41]. Another potential solution relies on exploiting some characteristics of metamaterials and/or periodic systems in combination with ABHs. In particular, locally resonant metamaterials [42] that involve periodically or randomly arranged resonators have proved very valuable to manipulate waves at low frequencies. Locally resonant metamaterials usually perform well in the frequency band where the resonators' eigen-frequencies belong, though some careful designs have been conceived to try to expand their effective frequency band [43–45]. To date, metamaterials have not only proved to be useful for vibration reduction [46–48], but for sound insulation [49, 50] and wave manipulation [51, 52] as well. It is therefore natural to wonder whether metamaterials could be employed to improve the performance of ABH plates at low frequencies. This was the proposal in [53], where periodically distributed damped resonators were added to an ABH plate and tuned at its first eigenfrequency. That metamaterial ABH plate design, which was referred to as the MMABH plate, presented substantial vibration reduction for the whole frequency range, from lower to higher frequencies. It is the purpose of this work to check whether the MMABH is also capable of broadband sound radiation reduction and, if this is the case, understand the reasons behind such behavior.

With the exception of [12, 25], in which impaired broadband sound radiation from a plate with periodically tunneled double-leaf ABHs was analyzed, and as far as the authors know no further works have contemplated the performance of enhanced ABH plates in terms of sound emission. For the time being, all the above cited papers have basically focused on achieving and analyzing broadband vibration reduction. As said, it is our goal in what follows to characterize the sound radiation from the MMABH plate. To start with, we will briefly summarize how to compute the vibration field of the MMABH plate, following the contents in [53]. Essentially, what it is done is to adapt our previously established Gaussian expansion method (GEM) [13, 16, 54] to incorporate local resonators by means of a simplified component mode synthesis (CMS) approach, which is beneficial because of model order reduction [55]. For brevity, the resulting numerical method will be hereafter termed as the GECMS. It is worth mentioning that the very recently developed nullspace method [56] could have been used instead to assemble substructures, yet this is left for future developments. Once we have the velocity distribution on the MMABH surface for a given external

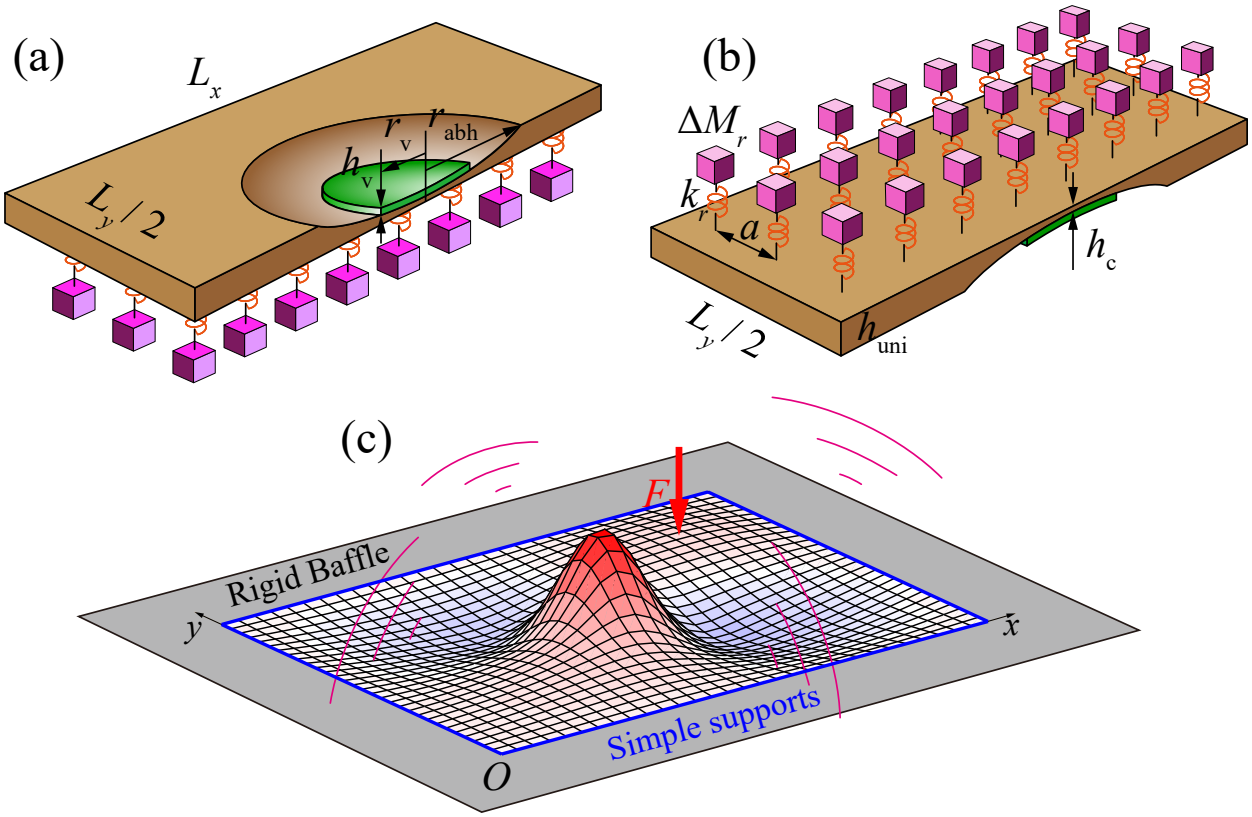

Figure 1: (a) 3D sectional view for the proposed MMABH plate, in which the green portion represents the damping layer. (b) The flat side of the MMABH plate, where the resonators are attached. (c) Discretized sound radiation model for the simply supported MMABH plate under a point force excitation and surrounded by an infinite rigid baffle.

excitation, the far-field acoustic pressure can be determined by means of Rayleigh's integral (see e.g., [22, 57–60]). By introducing a discrete radiation model and an associated resistance matrix, the sound power level and radiation efficiency of the MMABH plate can be computed, following the steps in [22, 61]. Finally, to determine which regions of the MMABH surface are responsible for the far-field sound radiation, we will resort to non-negative intensity (NNI) [62–65] as an alternative to supersonic intensity analysis [22, 66, 67] because of ease of implementation and slightly better performance at low frequecnies [68].

The paper is organized as follows. In Section 2 we describe the MMABH plate. In Section 3, we introduce all theoretical developments needed to analyze sound radiation from the MMABH. In particular, it is exposed how to obtain the MMABH vibration field and how to compute the far-field acoustic pressure, sound power level, radiation efficiency and non-negative intensity. Section 4 presents the results of the numerical simulations and analyze them in detail. Conclusions close the paper in Section 5. For completeness, Appendix A provides the mass and stiffness matrices, and the modal vectors, which are necessary to compute the MMABH surface velocity distribution. In Appendix B, the phenomena of bandgap formation and coincidence frequencies for the MMABH are explained and it is shown how they change depending on the lattice constant and plate thickness.

2. Design of the MMABH plate

A sketch of the MMABH plate proposed in [53] is shown in Figs. 1a and 1b. It consists of a uniform plate with a circular ABH indentation placed at its center and a regular lattice of local resonators distributed on its flat surface. The MMABH plate has dimensions $L_x \times L_y$ and the thickness outside the ABH is h_{uni}. The

Geometry parameters	Material parameters
$m = 2.5$	$\rho_p = 7800$ kg/m^3
$L_x = 0.8$ m	$E_p = 210$ GPa
$L_y = 0.6$ m	$\eta_p = 0.01$
$h_{\text{uni}} = 0.01$ m	$\nu_p = 0.3$
$r_{\text{abh}} = 0.24$ m	
$\varepsilon = 0.3189$ m$^{-1.5}$	$\rho_v = 950$ kg/m^3
$h_c = 0.001$ m	$E_v = 5$ GPa
$r_v = 0.12$ m	$\eta_v = 0.5$
$h_v = 0.001$ m	$\nu_v = 0.3$

Table 1: Geometry and material parameters of the ABH plate. ρ_p: plate density, ρ_v: damping layer density, E_p: plate Young modulus, E_v: damping layer Young modulus, η_p: plate loss factor, η_v: damping layer loss factor, ν_p: plate Poisson ratio, ν_v: damping layer Poisson ratio.

radius of the ABH is r_{abh} and the residual thickness at its center, (x_c, y_c), is denoted by h_c. The thickness profile of the ABH is given by $h(r) = \varepsilon r^m + h_c$, where ε stands for the ABH slope (smoothness parameter), m for the ABH order and $r = \sqrt{(x-x_c)^2 + (y-y_c)^2} < r_{\text{abh}}$ for the horizontal local distance. To dissipate energy, a circular thin viscoelastic layer of thickness h_v and radius r_v is attached at the center of the ABH. On the other hand, and as mentioned in the introduction, the ABH effect does not work to reduce low-frequency vibrations. This is the task of the local resonators, which are uniformly distributed on the plate (see Fig. 1b): n_x and n_y resonators are respectively placed in the x and y directions resulting in a total of $n_x \times n_y$ resonators. For simplicity, a square lattice is chosen with lattice constant $a = L_x/n_x = L_y/n_y$. The MMABH is designed so that its overall weight does not surpass that of the original uniform plate where we embed the ABH. Therefore, the mass removed to make the ABH indentation, ΔM, is recycled as that of the resonators, so each one has mass $\Delta M_r = \Delta M/(n_x n_y)$. The resonators have springs of identical stiffness $k_r = (2\pi f_r)^2 \Delta M_r$, f_r being their eigen-frequency. In this paper, we tune $f_r = f_1$, where f_1 stands for the first resonant frequency of the ABH plate. The values of the geometrical and physical parameters values of the MMABH used for the simulations in this paper are given in Table 1.

Let us also note that we are considering a design with a single ABH indentation for the MMABH plate. Given that the ABH cut-on frequency is given by $f_{\text{cut-on}} = \frac{\pi h_{\text{uni}}}{4 r_{\text{abh}}^2} \sqrt{\frac{E_p}{3\rho_p(1-\nu_p^2)}}$ it is clear that the larger the ABH radius, r_{abh}, the lower $f_{\text{cut-on}}$. Therefore, if we want to achieve vibration and noise radiation broadband frequency reduction is better to chose a single large ABH over several smaller ones [54]. Admittedly, in a real implementation this option could present some problems because of the plate stiffness would be weakened so, depending on the target, a metaplate with more than one ABH could be a reasonable option. However, we will not address this situation in this paper but focus on the design in Figs. 1a and 1b.

3. Characterization of sound radiation

3.1. Far field radiation

To perform sound radiation computations the MMABH vibrating surface is divided into N elementary radiators, each one having area ΔS. Within ΔS, the plate transverse velocity $v_p(\boldsymbol{x}_0) = \mathrm{i}\omega w_p(\boldsymbol{x}_0)$ is assumed to be constant. Here, $w_p(\boldsymbol{x}_0)$ denotes the vertical displacement at point $\boldsymbol{x}_0 = (x_0, y_0)$ on the plate. To avoid complications due to diffraction, the MMABH plate is set in an infinite rigid baffle, as illustrated in Fig. 1c.

The acoustic pressure at a far field point $\boldsymbol{x}$ for a given radian frequency ω can be obtained, as usual, by means of Rayleigh's integral,

$$p(\boldsymbol{x}) = \frac{\mathrm{i}\omega\rho_0}{2\pi} \int_0^{L_x} \int_0^{L_y} v_p(\boldsymbol{x}_0) \frac{\mathrm{e}^{-\mathrm{i}k\|\boldsymbol{x}-\boldsymbol{x}_0\|}}{\|\boldsymbol{x}-\boldsymbol{x}_0\|} \mathrm{d}x_0 \mathrm{d}y_0, \tag{1}$$

where $k = \omega/c_0$ is the wavenumber and c_0 and ρ_0 respectively represent the speed of sound and the air density. The integral in Eq. (1) can be computed by means of standard numerical techniques once the surface velocity distribution $v_p(\boldsymbol{x}_0)$ of the plate is known. Here $v_p(\boldsymbol{x}_0)$ could correspond to the velocity pattern of an MMABH plate mode, or to the velocity response to a given point or distributed external excitation. Obtaining $v_p(\boldsymbol{x}_0)$ for the MMABH plate is not straightforward, as finite element simulations become demanding due to the small value of the truncation thickness h_c at the center of the ABH. An alternative approach has been recently developed by the authors in [53]. The method is termed the GECMS and essentially consists in first using Gaussian functions as a basis in the framework of the Rayleigh-Ritz method to determine the modes of the bare ABH plate (i.e without resonators). A modal reduction of the model is then carried out and finally the resonators become attached to the plate by incorporating their influence in the Lagrangian of the overall system (i.e., the MMABH plate). In the following lines a brief overview of the GECMS is presented given that it will be used to get $v_p(\boldsymbol{x}_0)$ in the simulations of Section 4 below.

The starting point is to follow [13, 54] and expand the displacement field of the bare ABH plate as

$$w_p(\boldsymbol{x}_0, t) = \boldsymbol{a}^\top(t)\boldsymbol{\chi}(\boldsymbol{x}_0) = \boldsymbol{\chi}^\top(\boldsymbol{x}_0)\boldsymbol{a}(t), \tag{2}$$

where $\boldsymbol{\chi}(\boldsymbol{x}_0)$ represents a vector of basis Gaussian functions and $\boldsymbol{a}(t)$ their corresponding time-dependent coefficient vector. We can use this expansion to write the Lagrangian of the ABH plate as

$$\mathscr{L} = T_p - V_p = \frac{1}{2}\dot{\boldsymbol{a}}^\top \boldsymbol{M}_p \dot{\boldsymbol{a}} - \frac{1}{2}\boldsymbol{a}^\top \boldsymbol{K}_p \boldsymbol{a}, \tag{3}$$

where T_p and V_p respectively stand for the bare ABH plate kinetic and potential energy, and $\boldsymbol{M}_p$ and $\boldsymbol{K}_p$ are their corresponding mass and stiffness matrices (see Appendix A). If we next apply the Euler-Lagrange equations, $\partial_t(\partial_{\dot{\boldsymbol{a}}}\mathscr{L}) - \partial_{\boldsymbol{a}}\mathscr{L} = 0$, to Eq. (3) and consider the time harmonic dependence $\boldsymbol{a}(t) = \hat{\boldsymbol{A}}\exp(\mathrm{i}\omega t)$, we get the eigenvalue problem, $\left[-\omega^2\boldsymbol{M}_p + \boldsymbol{K}_p\right]\hat{\boldsymbol{A}} = \boldsymbol{0}$, from which we obtain the bare ABH plate eigenvectors $\hat{\boldsymbol{A}}_i$, $i = 1 \dots N$. Let us only select those necessary to cover the frequency range of interest, say the first $\overline{N}$ ones. In most practical cases $\overline{N} \ll N$ which substantially reduces the dimensions of the problem. To avoid confusions, the selected eigenvectors will be written as $\overline{\boldsymbol{A}}_i$, $i = 1 \dots \overline{N}$. If $\overline{\boldsymbol{P}}$ stands for the eigenmatrix containing all $\overline{\boldsymbol{A}}_i$ in columns, we can obtain the generalized mass and stiffness matrices $\overline{\boldsymbol{M}}_p = \overline{\boldsymbol{P}}^\top \boldsymbol{M}_p \overline{\boldsymbol{P}}$ and $\overline{\boldsymbol{K}}_p = \overline{\boldsymbol{P}}^\top \boldsymbol{K}_p \overline{\boldsymbol{P}}$. Introducing modal coordinates such that, $\boldsymbol{a} = \overline{\boldsymbol{P}}\boldsymbol{\varepsilon}_p$, the Lagrangian in Eq. (3) transforms (in the considered frequency range) to

$$\mathscr{L} \approx \overline{\mathscr{L}} = \overline{T_p} - \overline{V_p} = \frac{1}{2}\dot{\boldsymbol{\varepsilon}}_p^\top \overline{\boldsymbol{M}}_p \dot{\boldsymbol{\varepsilon}}_p - \frac{1}{2}\dot{\boldsymbol{\varepsilon}}_p^\top \overline{\boldsymbol{K}}_p \dot{\boldsymbol{\varepsilon}}_p. \tag{4}$$

We are now in disposition to account for the influence of the resonators on the plate. This is done by adding their kinetic energy to $\overline{T_p}$ and the potential one to $\overline{V_p}$, namely,

$$\overline{T} = \overline{T_p} + \sum_{i=1}^{n_x n_y} T_{ri} = \frac{1}{2}\dot{\boldsymbol{\varepsilon}}_p^\top \overline{\boldsymbol{M}}_p \dot{\boldsymbol{\varepsilon}}_p + \sum_{i=1}^{n_x n_y} \frac{1}{2}\dot{\overline{w}}_{ri}\dot{\overline{w}}_{ri} = \frac{1}{2}\dot{\boldsymbol{\varepsilon}}^\top \overline{\boldsymbol{M}}\dot{\boldsymbol{\varepsilon}}, \tag{5}$$

$$\overline{V} = \overline{V_p} + \sum_{i=1}^{n_x n_y} V_{ri} = \frac{1}{2}\boldsymbol{\varepsilon}_p^\top \overline{\boldsymbol{K}}_p \boldsymbol{\varepsilon}_p + \sum_{i=1}^{n_x n_y} \frac{1}{2}\boldsymbol{\varepsilon}^\top \overline{\boldsymbol{K}}_{ri}\boldsymbol{\varepsilon} = \frac{1}{2}\boldsymbol{\varepsilon}^\top \overline{\boldsymbol{K}}\boldsymbol{\varepsilon}. \tag{6}$$

In Eq. (5) and Eq. (6), T_{ri} and V_{ri} respectively stand for the kinetic and potential energy of the i-th resonator, $\overline{w}_{ri} = w_{ri}/\sqrt{m_i}$ denote its normalized displacement and $\overline{\boldsymbol{K}}_{ri}$, $\overline{\boldsymbol{K}}$ and $\overline{\boldsymbol{M}}$ represent appropriate stiffness and mass matrices whose expressions are provided in Appendix A. From Eqs. (5) and (6) we can finally build the MMABH plate Lagrangian, namely,

$$\mathscr{L}_{\mathrm{MMABH}} = \overline{T} - \overline{V} = \frac{1}{2}\dot{\boldsymbol{\varepsilon}}^\top \overline{\boldsymbol{M}}\dot{\boldsymbol{\varepsilon}} - \frac{1}{2}\boldsymbol{\varepsilon}^\top \overline{\boldsymbol{K}}\boldsymbol{\varepsilon}, \tag{7}$$

and applying the Euler-Lagrange equations again, while assuming $\boldsymbol{\varepsilon}(t) = \hat{\boldsymbol{\varepsilon}}\exp(\mathrm{i}\omega t)$, we get the eigenvalue problem

$$\left(-\omega^2\overline{\boldsymbol{M}} + \overline{\boldsymbol{K}}\right)\hat{\boldsymbol{\varepsilon}} = \boldsymbol{0}, \tag{8}$$

from which we can compute the modes of the MMABH plate. In the case of an external force excitation, $\boldsymbol{f}$, the plate response is obtained through modal superposition.

For the radiation problem, once we get the flexural displacement of the MMABH plate, $w_p(x, y)$, from Eq. (B.5), we can compute its mean value for each radiator ΔS and arrange the result in a vector, $\boldsymbol{w}_p$, having as much rows as radiators in the plate. The velocity vector to be used in the discrete version of Eq. (1) is then given by $\boldsymbol{v}_p = \mathrm{i}\omega\boldsymbol{w}_p$.

3.2. Sound power and radiation efficiency

The radiated sound power, W_{rad}, of the MMABH plate is given by,

$$W_{\mathrm{rad}} = \frac{\Delta S}{2}\mathrm{Re}\left(\boldsymbol{v}_p^{\mathrm{H}}\boldsymbol{p}_p\right), \tag{9}$$

where $\boldsymbol{p}_p$ is the $N \times 1$ vector containing the acoustic surface pressure of each radiator and the superscript H stands for the Hermitian (complex conjugation plus transposition). In order to obtain W_{rad} solely in terms of the surface velocity, $\boldsymbol{v}_p$, we introduce the impedance matrix, $\boldsymbol{Z}$, such that (see [69]),

$$\boldsymbol{p}_p = \boldsymbol{Z}\boldsymbol{v}_p, \tag{10}$$

with

$$\boldsymbol{Z} = \rho_0 c_0 \begin{bmatrix} d & \frac{-\mathrm{i}k\Delta S}{2\pi}\frac{\mathrm{e}^{\mathrm{i}kr_{12}}}{r_{12}} & \cdots & \frac{-\mathrm{i}k\Delta S}{2\pi}\frac{\mathrm{e}^{\mathrm{i}kr_{1N}}}{r_{1N}} \\ \frac{-\mathrm{i}k\Delta S}{2\pi}\frac{\mathrm{e}^{\mathrm{i}kr_{21}}}{r_{21}} & d & \cdots & \vdots \\ \vdots & \vdots & \ddots & \vdots \\ \frac{-\mathrm{i}k\Delta S}{2\pi}\frac{\mathrm{e}^{\mathrm{i}kr_{N1}}}{r_{N1}} & \cdots & \cdots & d \end{bmatrix}. \tag{11}$$

Here, $r_{mn} = r_{nm}$ $(1 \leq m, n \leq N)$ is the shortest surface distance between radiators m and n. When $m = n$, the diagonal terms d in Eq. (11) become singular. One can avoid the singularity by integrating over a circular area around the center of the radiator to get [69, 70],

$$d = \frac{1}{2}\left(k\sqrt{\frac{\Delta S}{\pi}}\right)^2 - \mathrm{i}\frac{8}{3\pi}\left(k\sqrt{\frac{\Delta S}{\pi}}\right). \tag{12}$$

Using Eqs. (10) and (11), the radiated sound power in Eq. (9) can be expressed as

$$W_{\mathrm{rad}} = \frac{\Delta S}{2}\mathrm{Re}\left(\boldsymbol{v}_p^{\mathrm{H}}\boldsymbol{p}_p\right) = \frac{\Delta S}{2}\mathrm{Re}\left(\boldsymbol{v}_p^{\mathrm{H}}\boldsymbol{Z}\boldsymbol{v}_p\right) = \boldsymbol{v}_p^{\mathrm{H}}\mathrm{Re}\left(\frac{\boldsymbol{Z}}{2}\right)\boldsymbol{v}_p\Delta S \equiv \boldsymbol{v}_p^{\mathrm{H}}\boldsymbol{R}\boldsymbol{v}_p\Delta S, \tag{13}$$

where in the last equality we have introduced the real symmetric and positive-definite resistance matrix $\boldsymbol{R}$,

$$\boldsymbol{R} = \frac{\omega^2\rho_0\Delta S}{4\pi c_0}\begin{bmatrix} 1 & \frac{\sin(kr_{12})}{kr_{12}} & \cdots & \frac{\sin(kr_{1N})}{kr_{1N}} \\ \frac{\sin(kr_{21})}{kr_{21}} & 1 & \cdots & \vdots \\ \vdots & \vdots & \ddots & \vdots \\ \frac{\sin(kr_{N1})}{kr_{N1}} & \cdots & \cdots & 1 \end{bmatrix}. \tag{14}$$

The radiation efficiency of the MMABH plate is finally obtained from [71],

$$\sigma = \frac{W_{\mathrm{rad}}}{\rho_0 c_0 N\Delta S\langle v^2\rangle_{\mathrm{MMABH}}} = \frac{W_{\mathrm{rad}}}{\rho_0 c_0\Delta S\boldsymbol{v}_p^{\mathrm{H}}\boldsymbol{v}_p}, \tag{15}$$

where $\langle v^2\rangle_{\mathrm{MMABH}}$ designates the mean square velocity (MSV) over the MMABH plate surface.

3.3. Non-negative intensity

To fully characterize the sound radiation behaviour of the MMABH plate it does not suffice to provide its sound power level and radiation efficiency. One also needs to know which regions of the plate are responsible for sound radiation at each frequency. It turns out that sound intensity is inefficient to that goal because the contributions from neighboring radiators with positive and negative values cancel out. That problem led to the development of supersonic intensity [66, 72], in which the acoustic pressure and velocity are transformed to the wavenumber domain and the subsonic components responsible for near field evanescent waves are filtered out. Supersonic intensity in the spatial domain was lately proposed for planar [67] and cylindrical [61] surfaces, based on convolution operations. However, supersonic intensity can still show positive and negative values and as an alternative, the concept of non-negative intensity (NNI) was introduced in [73]. NNI relies on acoustic radiation modes and it is easy to implement. It has been recently shown that NNI is very suitable to locate sound source at low frequencies [68], therefore in this work we will use it to determine the effective radiation regions of the MMABH plate.

The essentials of the NNI rely on finding the eigenpairs $(\lambda_i, \boldsymbol{\Psi}_i)$ of the resistance matrix $\boldsymbol{R}$ in Eq. (14) (see [73]). Note that all λ_i are strictly positive because $\boldsymbol{R}$ is a positive-definite matrix. The eigenvalues and eigenvectors of $\boldsymbol{R}$ can be grouped in matrices

$$\begin{aligned} \boldsymbol{\Lambda} &= \mathrm{diag}(\lambda_1, \lambda_2, \lambda_3, ..., \lambda_i, ..., \lambda_N), \\ \boldsymbol{\Psi} &= [\boldsymbol{\Psi}_1, \boldsymbol{\Psi}_2, \boldsymbol{\Psi}_3, ..., \boldsymbol{\Psi}_i, ..., \boldsymbol{\Psi}_N], \end{aligned} \tag{16}$$

with $\boldsymbol{\Psi}_i$ normalized such that

$$\begin{aligned} \boldsymbol{\Psi}^\top \boldsymbol{\Psi} &= \boldsymbol{I}, \\ \boldsymbol{\Psi}^\top \boldsymbol{R} \boldsymbol{\Psi} &= \boldsymbol{\Lambda}. \end{aligned} \tag{17}$$

Eq. (17) allows one to re-express the resistance matrix as

$$\boldsymbol{R} = \boldsymbol{\Psi}\boldsymbol{\Lambda}\boldsymbol{\Psi}^\top = \boldsymbol{\Psi}\sqrt{\boldsymbol{\Lambda}}\sqrt{\boldsymbol{\Lambda}}\boldsymbol{\Psi}^\top = \boldsymbol{\Psi}\sqrt{\boldsymbol{\Lambda}}\left(\boldsymbol{\Psi}^\top\boldsymbol{\Psi}\right)\sqrt{\boldsymbol{\Lambda}}\boldsymbol{\Psi}^\top = \left(\boldsymbol{\Psi}\sqrt{\boldsymbol{\Lambda}}\boldsymbol{\Psi}^\top\right)\left(\boldsymbol{\Psi}\sqrt{\boldsymbol{\Lambda}}\boldsymbol{\Psi}^\top\right) \equiv \boldsymbol{\Phi}^\top\boldsymbol{\Phi}, \tag{18}$$

which shows that $\boldsymbol{R}$ can be factorized as the product of two identical matrices. Taking Eq. (18) into Eq. (13) yields the following result for the radiated sound power

$$W_{\mathrm{rad}} = \boldsymbol{v}_p^{\mathrm{H}}\boldsymbol{R}\boldsymbol{v}_p\Delta S = \boldsymbol{v}_p^{\mathrm{H}}\boldsymbol{\Phi}^\top\boldsymbol{\Phi}\boldsymbol{v}_p\Delta S = \left(\boldsymbol{\Phi}\boldsymbol{v}_p\right)^{\mathrm{H}}\left(\boldsymbol{\Phi}\boldsymbol{v}_p\right)\Delta S \equiv \boldsymbol{\beta}^{\mathrm{H}}\boldsymbol{\beta}\Delta S. \tag{19}$$

In the last equality of Eq. (19) we have identified the vector $\boldsymbol{\beta}$. The i-th entry of this vector, β_i, represents the square root of the NNI of the i-th radiator. In other words, the sound intensity of the i-th elementary radiator is given by the square of β_i, which makes it inevitably non-negative. The NNI vector can therefore be defined as

$$\boldsymbol{I}_p^{\mathrm{NNI}} = \boldsymbol{\beta}^* \odot \boldsymbol{\beta}, \tag{20}$$

where $\odot$ symbolizes the Hadamard product (entrywise) and the superscript $*$ designates the complex conjugate.

4. Numerical results

4.1. MMABH plate features

For the numerical simulations, hereafter we will consider an MMABH plate having the geometrical and physical parameters listed in Table 1. As explained in Section 2, the mass removed from the plate when fabricating the ABH, $\Delta M = 7.0573$ kg, becomes distributed between all resonators. We chose a total of $n_x \times n_y = 16 \times 12 = 192$ resonators, each one having equal mass $\Delta M_r = \Delta M/192 = 0.0368$ kg, and with lattice constant $a = 0.05$ m. The first resonant frequency of the bare ABH plate is $f_1 = 96.7$ Hz, which implies each resonator has stiffness $k_r = (2\pi f_1)^2 \Delta M_r = 13569$ N/m. An external point force of amplitude 1 N is exerted at the location (0.725, 0.55) m and the MMABH plate is assumed to be simply supported at its boundaries.

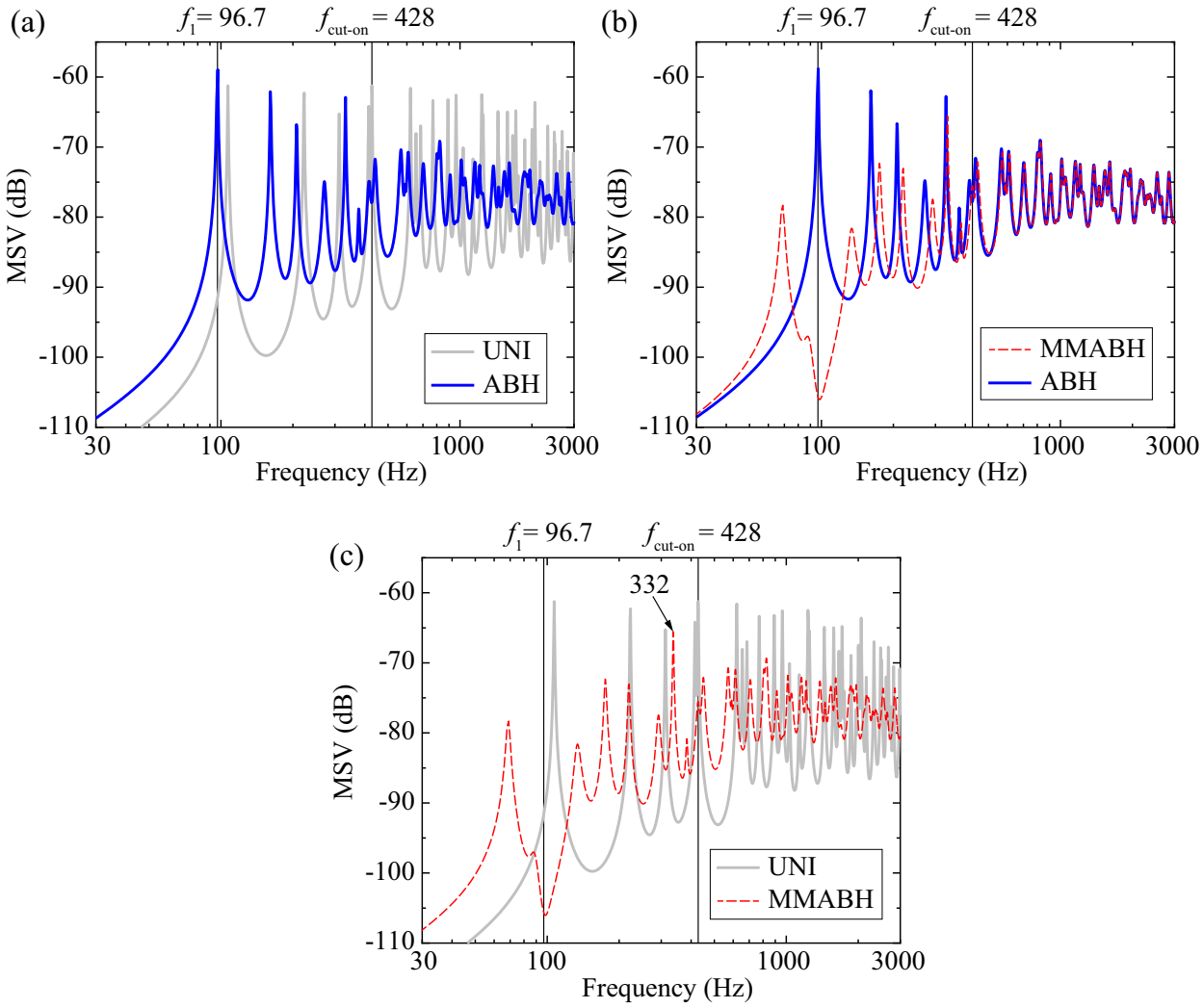

Figure 2: Mean square velocity (MSV) comparison between (a) the ABH and UNI plates, (b) the MMABH and ABH plates and (c) the MMABH and UNI plates. The reference velocity is selected as 1 m/s.

4.2. Surface vibration of the MMABH

The velocity distribution on the plate surface, $v_p(\boldsymbol{x}_0)$, turns to be one of the utmost variables for sound radiation as it appears in the formula for the far-field radiation, Eq. (1), in that of the sound power level, Eq. (9), radiation efficiency, Eq. (15), and non-negative intensity, Eqs. (19) and (20). Although the vibration reduction when exciting the MMABH plate in comparison to an ABH plate or a uniform one has been analyzed in detail in [53], it is worth illustrating here some basic results for completeness. We focus on the surface mean square velocity (MSV) of those plates, defined as $\mathrm{MSV(dB)} = 10\log\left[\omega^2 \int_0^{L_x}\int_0^{L_y} w^2(x_0,y_0)\mathrm{d}y_0\mathrm{d}x_0/(L_xL_y)\right]$. In Fig. 2a, we compare the MSV of an ABH plate with that of a uniform plate (having the same amount of damping) and observe the well-known ABH effect. Beyond the ABH cut-on frequency, $f_{\mathrm{cut-on}} = 428$ Hz, the vibration gets substantially reduced (up to ~ 10 dB), but for lower frequencies there is no improvement with respect to the uniform plate. This is known to be the main drawback of ABH designs. The MMABH plate was intended to remedy this situation. If we add 16×12 resonators tuned at the first resonance of the ABH plate, namely $f_1 = 96.7$ Hz, it is observed how the vibration attenuation is also remarkable at low frequencies thanks to bandgap formation, see Fig. 2b and the explanations in Appendix B. It is to be

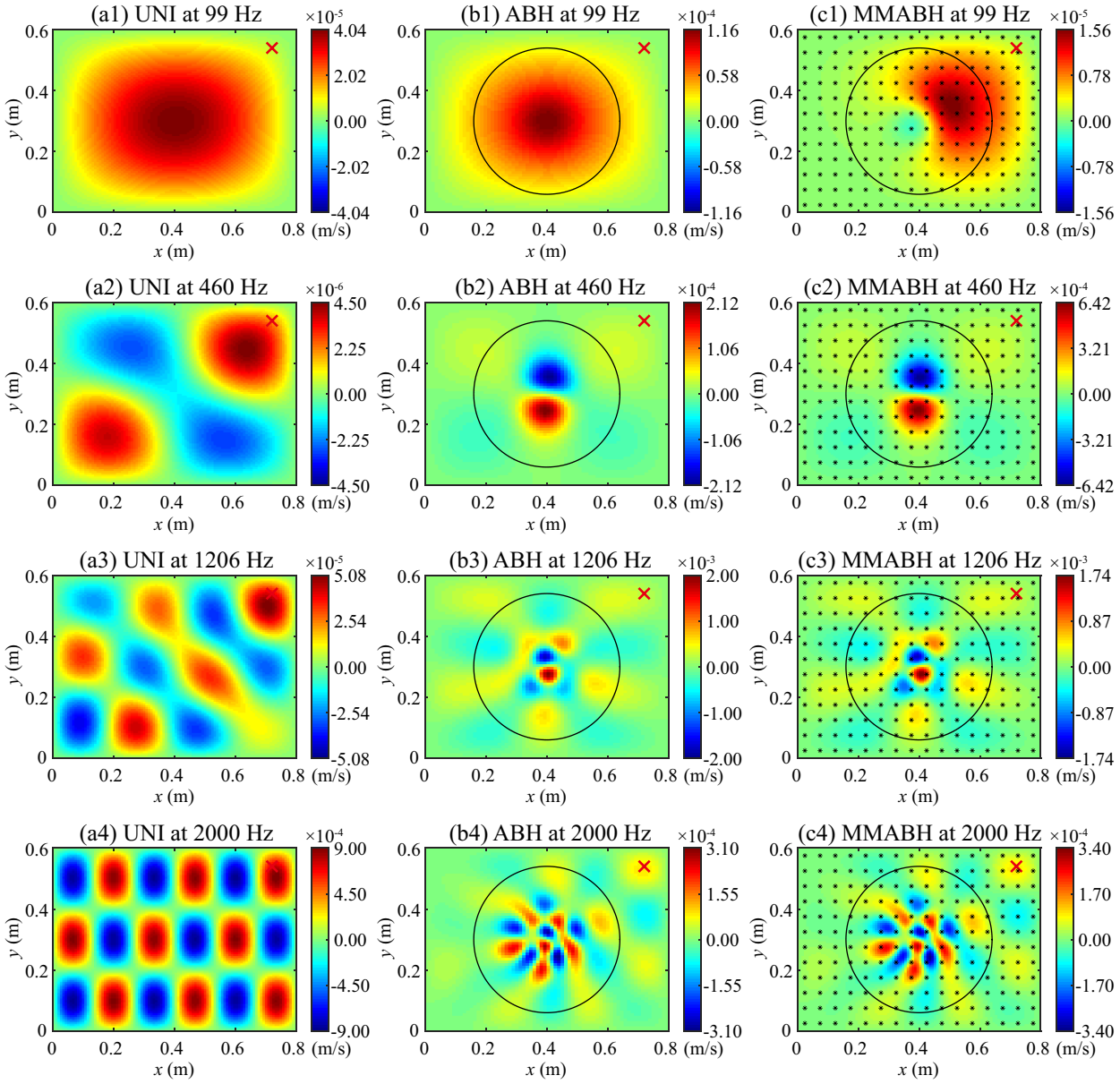

Figure 3: Velocity distribution on the surface of (a1)-(a4) the UNI plate, (b1)-(b4) ABH plate, and (c1)-(c4) MMABH plate, at different frequencies. The black asterisks in the last column stand for the location of the resonators. The red crosses in each subfigure symbolize the external point force. Different color scales are used to better appreciate the results.

noticed that the resonators have to be properly damped to diminish all other peaks but f_1, see [74]. In this paper we have considered a loss factor of $\eta_r = 0.1$ for the stiffness of each resonator, i.e., $k_r = k_r(1 + \mathrm{i}\eta_r)$. To finally highlight the better performance of the MMABH plate in front of a uniform one with identical weight, in Fig. 2c we present their corresponding MSVs. It is observed that the MMABH plate lowers almost all peaks in the analyzed frequency range. The sole exception is that at $f = 332$ Hz. This peak could be also smoothed by including additional resonators tuned at its particular frequency though this is deemed out of the scope of this work. Beyond this, it becomes apparent from Fig. 2 that the MMABH plate offers clear advantages in terms of broadband vibration reduction.

To gain some more insight on how the MMABH helps reducing vibrations, we can next have a look at the

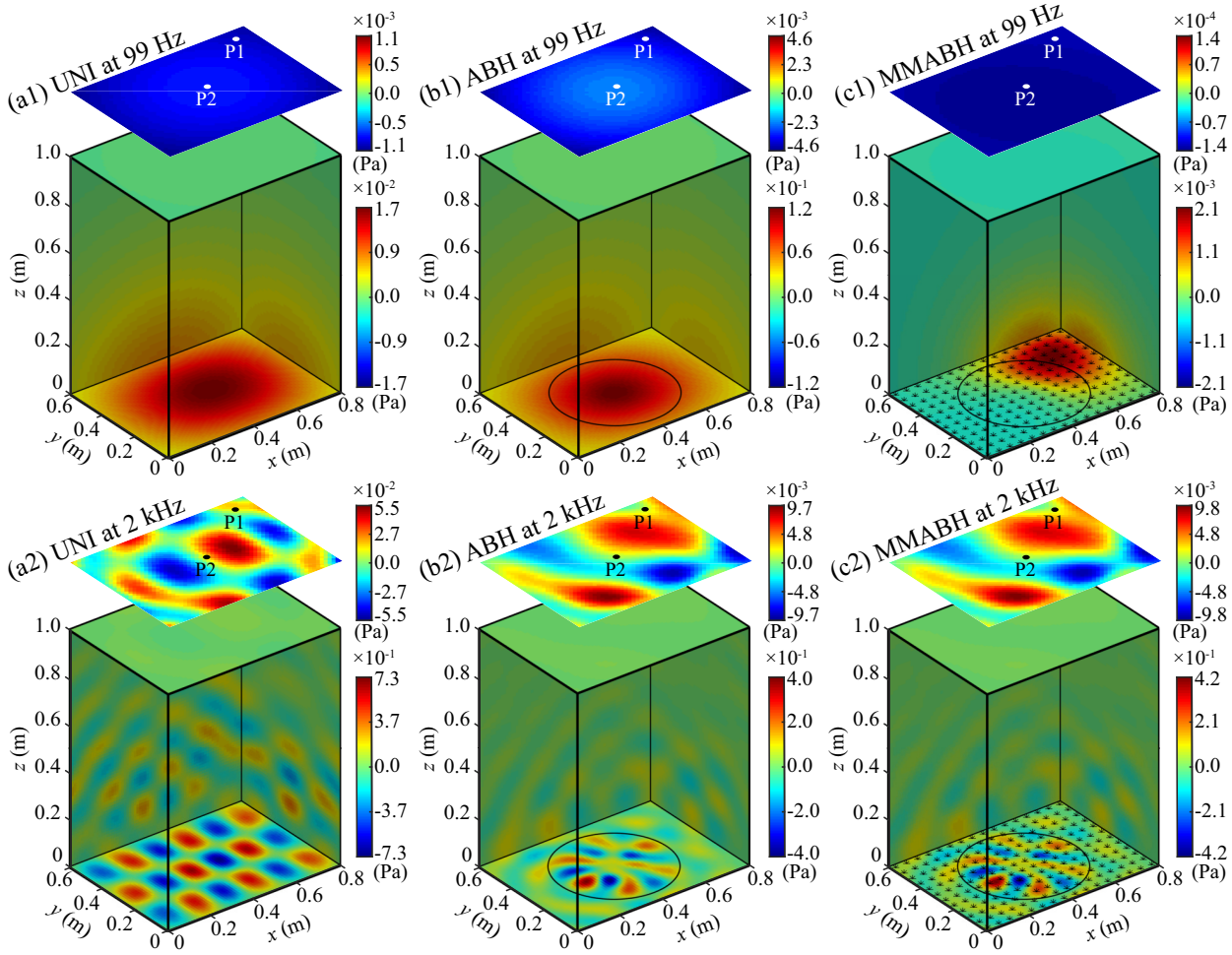

Figure 4: Far-field acoustic pressure radiated by (a1)-(a2) the UNI plate, (b1)-(b2) the ABH plate, and (c1)-(c2) the MMABH plate, at frequencies $f = 99$ Hz (first row) and $f = 2000$ Hz (second row). Note that the top surface in each subfigure ($z = 1$ m) has been reproduced in a different color scale to better appreciate the values in it. P1 and P2 are two test points at (0.725, 0.55, 1) m and (0.4,0.3,1) m for which results are presented in Fig. 5.

plate surface velocity distribution for different frequencies. The three columns in Fig. 3 respectively present results for the uniform, ABH, and MMABH plates, while the rows correspond to different frequencies. Let us first inspect the first row in the figure, whose frequency $f = 99$ Hz is located inside the bandgap induced by the periodic distribution of resonators (see Appendix B). From Figs. 3a1 and 3b1 it is seen that the vibration patterns of the uniform plate and the ABH plate are very similar though the latter exhibits much stronger levels. The ABH effect does not work for such a low frequency and the reduction in stiffness due to the ABH indentation induces a very high vibration level. However, when adding the local resonators to the ABH plate the resulting MMABH one reduces the vibration of the ABH plate in $\sim 1/10$, see Fig. 3c1. Moreover, the wave propagating to the left from the excitation point gets stopped thanks to the bandgap formation. If we next consider the higher frequency $f = 460$ Hz, which is slightly higher than $f_{\mathrm{cut-on}} = 428$ Hz (second row in the figure), we observe how the vibration concentrates within the ABH region where it gets dissipated by the damping layer. The MMABH performs similarly to the ABH plate because the driving frequency is far from the eigen-frequency of the resonators. A similar behavior can be appreciated as long as the frequency increases, as seen in the third and fourth rows of the figure corresponding to $f = 1206$ Hz and $f = 2000$ Hz.

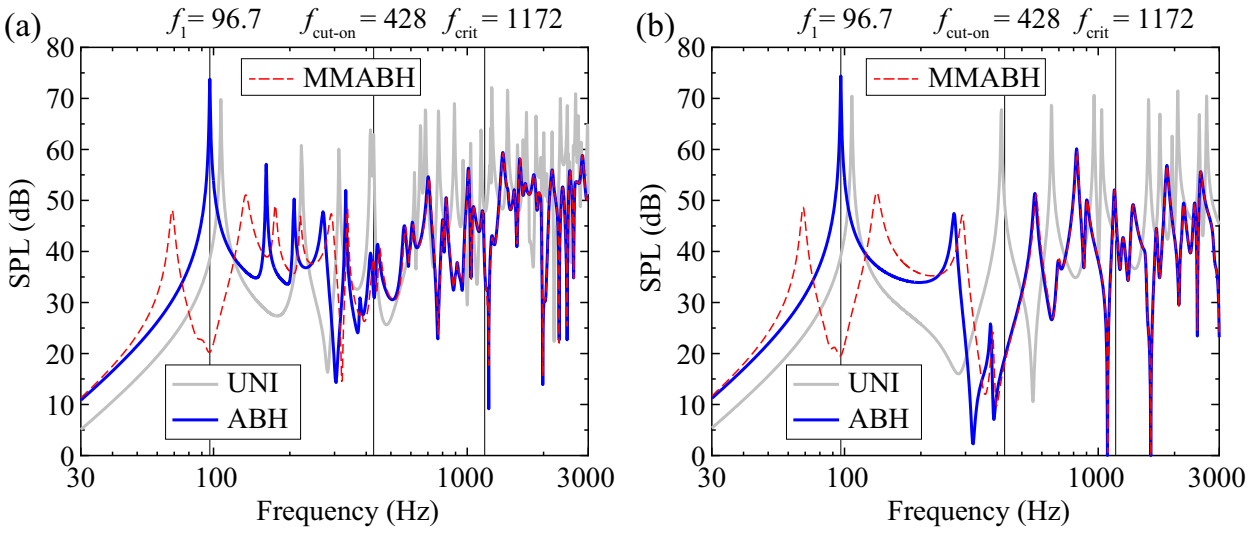

Figure 5: Far-field sound pressure level (SPL) at points (a) P1 and (b) P2 in Fig. 4.

4.3. Far-field radiation of the MMABH

Once obtained the velocity distribution on the plate surface we can compute the far-field acoustic pressure using Eq. (1). In Fig. 4, each column presents the sound pressure distribution radiated by the uniform (UNI), ABH and MMABH plates in a three-dimensional volume of $(0, 0.8) \times (0, 0.6) \times (0, 1)$ m^3 for two different frequencies, $f = 99$ Hz (first row) and $f = 2000$ Hz (second row). It can be seen from the figure that the sound pressure values decrease significantly as the distance from the source surface augments, as one would expect. To better highlight the sound pressure at the plane $z = 1$ m, we have redrawn the results for the top volume surface on each subplot. As observed, for $f = 99$ Hz, the far-field sound pressure of the ABH plate (4.6×10^{-3} Pa) is greater than that of the UNI one (1.1×10^{-3} Pa), because, as explained in the preceding section, the ABH effect does not work for this low frequency and the ABH plate is less rigid than the uniform one. As opposed, the sound radiated by the MMABH plate is about one order of magnitude (1.4×10^{-4} Pa) lower than those of the ABH and UNI plates. It is therefore clear that the MMABH significantly diminishes the far-field acoustic radiation of the ABH plate at low frequencies, thanks to the local resonators. For the higher frequency of 2000 Hz in the second row of the figure, the far-field radiation of the MMABH and ABH plates are almost identical and significantly smaller than that of the UNI one, indicating that the noise reduction effect at high frequencies is mainly due to the ABH effect.

On the other hand, in Fig. 5 we have depicted the sound pressure level (SPL) curves of the MMABH plate at test points P1 (0.725,0.55,1) m and P2 (0.4,0.3,1) m indicated in Fig. 4. These two points are respectively located just above the excitation force and above the centre of the ABH. Their SPLs are plotted in Figs. 5a and 5b and compared to those of the ABH and UNI plates. As seen from the two subfigures, the MMABH is able to substantially improve the behavior of the ABH plate at low frequencies while keeping its good performance at higher frequencies. It also overcomes the UNI plate for the whole frequency range.

4.4. Surface sound pressure, sound power level and radiation efficiency of the MMABH

To further understand how the MMABH radiates sound, we next analyze its surface sound pressure distribution, sound power level and radiation efficiency, following the developments in Section 3.2.

The sound pressure on the MMABH surface corresponding to the vibration fields plotted in the subfigures of Fig. 3 is computed from Eq. (10) and plotted in Fig. 6. As seen in the first row, for 99 Hz the sound pressure patterns of the uniform and the ABH plates are very similar (see Figs. 6a1 and 6b1), with the largest values found at the plate centers. In fact, the maximum sound pressure for the ABH plate is almost 10 times bigger than that of the uniform plate. Again, this is attributed to the small rigidity induced by the

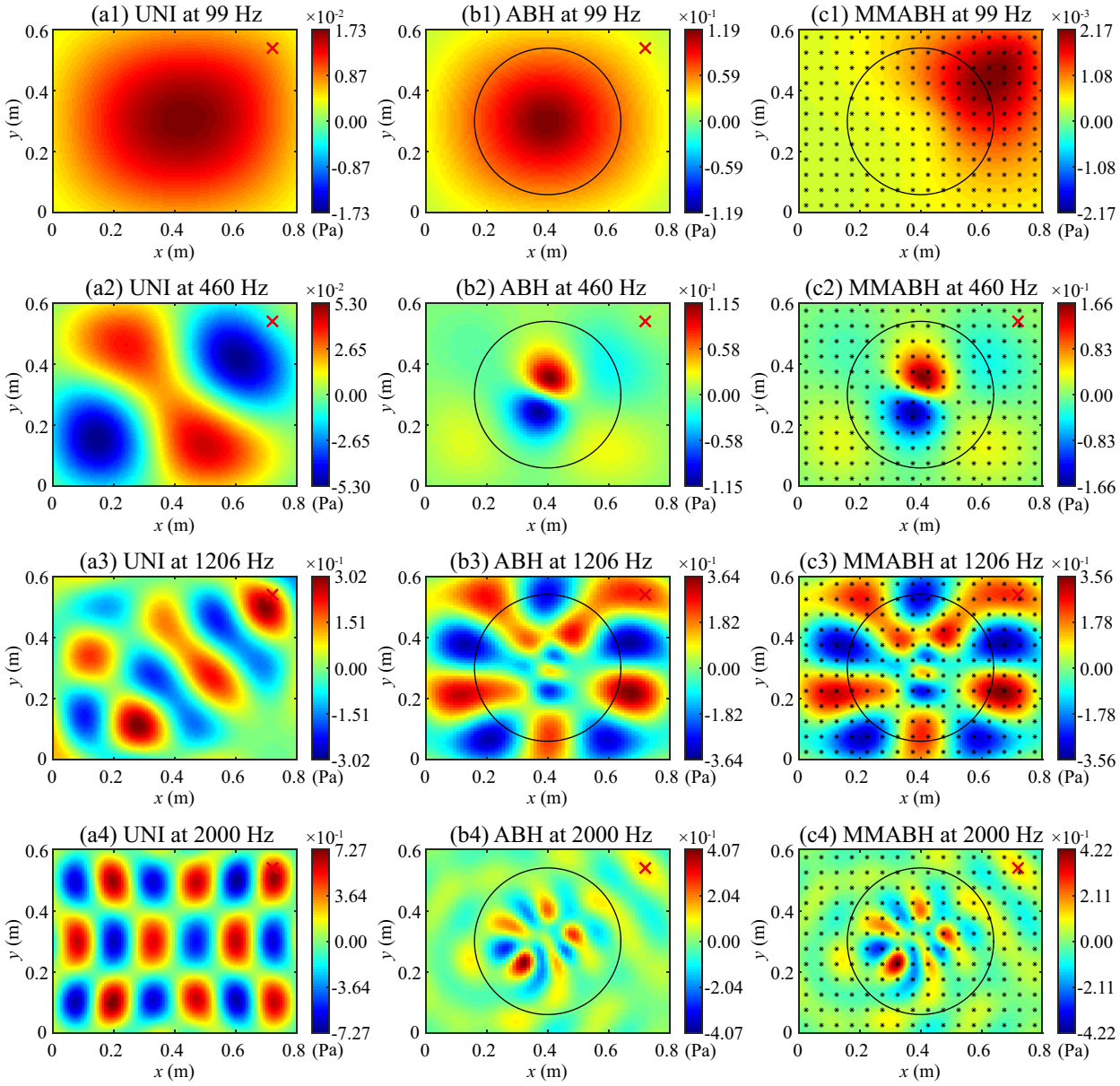

Figure 6: Sound pressure distribution on the surface of (a1)-(a4) the UNI plate, (b1)-(b4) ABH plate, and (c1)-(c4) MMABH plate, at different frequencies. Different color scales are used to better appreciate the results.

ABH indentation and has nothing to do with the ABH effect. As opposed, a drastic reduction of surface acoustic pressure is achieved for the MMABH plate because 99 Hz lies in the bandgap induced by the resonators. The maximum pressure levels are found close to the force excitation point with an amplitude $\sim$1/100 smaller than that of the ABH plate. This result confirms the usefulness of the resonators. Besides, in the second row of Fig. 6 we plot again the outcomes for 460 Hz, which is higher than the ABH cut-on frequency. In this case the maximum sound pressure is found in the ABH area for the ABH and MMABH plates as most vibration concentrates therein because of the ABH effect (see Figs. 6b2 and 6c2 and compare with the uniform plate in Fig. 6a2). The resonators have little impact on the pressure as seen from Fig. 6c2. At 1206 Hz, which is close to the critical frequency $f_{\text{crit}} = 1172$ Hz, the sound pressure on the three plates

augments. For the ABH and MMABH plates, very significant sound pressure levels are found outside the ABH region because the wavenumber in the uniform portion of the plate is close to that in air (see Appendix B). For very high frequencies, as 2000 Hz in the fourth row, the coincidence effect disappears and the sound pressure concentrates again inside the ABH area. Observe that the last row in Fig. 6 shows the sound pressures distributions we already depicted at the bottom surfaces of the radiation volumes in Fig. 4.

The sound power level (SWL) for the three plates is calculated from Eq. (13). In Fig. 7a, we compare the SWL radiated by the uniform plate with that of an ABH plate. It is seen that the ABH SWL for frequencies higher than $f_{\text{cut}-\text{on}} = 428$ Hz is strongly reduced, whereas no significant reduction is achieved at low frequencies (see e.g., the peak at $f_1 = 96.7$ Hz), as one could have expected [22]. In contrast, the MMABH plate also presents a noticeable SWL reduction at low frequencies, see Fig. 7b. It is seen in the figure, where the MMABH SWL is compared to the ABH one, that the influence of the local resonators in the SWL is noticeable and does not undermine the good performance of the ABH at higher frequencies. As pointed out in [53], the local resonance and ABH effects are very weakly coupled (at least for the present example). Finally, comparing the SWL of the uniform plate with that of the MMABH one in Fig. 7c, we observe the great potential of the MMABH plate as an average reduction of SWL close to $\sim$20 dB is attained.

Some additional insight on how the MMABH plate achieves such remarkable SWL reduction can be found by analyzing its radiation efficiency, which is computed from Eq. (15). In Fig. 8, we have plotted four different radiation efficiency curves. That with the UNI legend corresponds to a uniform plate while MMUNI indicates a uniform plate with attached local resonators. The figure also contains results for the ABH and MMABH plates. If we first compare the UNI and MMUNI radiation efficiencies, it is observed that the UNI curve follows the typical trend of increasing its value until the critical frequency is reached, and then starts diminishing. The MMUNI curve presents the same behavior except for frequencies close to f_1, where it has a dip and then slightly surpasses the values of the UNI plate. This can be attributed to the low-frequency coincidence phenomenon reported in Appendix B. If we now compare the UNI and MMUNI curves with the ABH and MMABH ones, it becomes clear that the ABH indentation has a profound impact on the radiation efficiency at almost all frequencies. Besides, focusing on the ABH and MMABH curves, it is seen that the radiation efficiency of the MMABH has a strong dip close to f_1, but becomes larger than that of the ABH plate for frequencies between f_1 and $f_{\text{cut}-\text{on}}$. Again, this is a consequence of the low-frequency coincidence effect, see Appendix B.

4.5. Sound intensity and non-negative intensity of the MMABH

In this section, we investigate which parts of the MMABH are responsible for the far-field sound radiation, by means of the non-negative intensity (NNI) introduced in Section 4.5. The results will be compared to those of the UNI and ABH plates at the previously considered frequencies $f = \{99, 460, 1206, 2000\}$ Hz. Let us start presenting results for the standard acoustic intensity and see why it fails (see e.g., [66, 73]). The surface acoustic intensity is shown in Fig. 9 for the three plates and four frequencies. At the lowest frequency of the figure, namely 99 Hz (first row), the maximum intensity values concentrate at the central region for the three plates, yet those of the MMABH one are much smaller than those of the UNI and ABH plates (the ABH values being the biggest). Note that the acoustic intensity of the UNI and ABH plates is almost positive at all surface points for such low frequency, but shows negative values for the MMABH. The situation drastically changes at 460 Hz (second row). In this case, the sound intensity of the ABH and MMABH plates focuses in the ABH center, while this is certainly not the case for the UNI one in Fig. 9a2. In all plots negative values of the acoustic intensity become significant indicating recirculating zones which do not radiate sound outwards. If we increase the frequency to 1206 Hz (third row in Fig. 9), the intensity of the ABH and MMABH plates present very high values in their uniform areas, because we are close to the uniform plate's critical frequency. Finally, at 2000 Hz (last row) very complex recirculation takes place in the ABH regions with alternating zones of positive and negative intensity.

While the acoustic intensity may give some hints on how the MMABH radiates sound, it is clear from the results in Fig. 9 that one should resort to supersonic (SSI) or to non-negative intensity (NNI) to correctly discriminate which zones in the plate are responsible for the far-field acoustic radiation, and avoid the

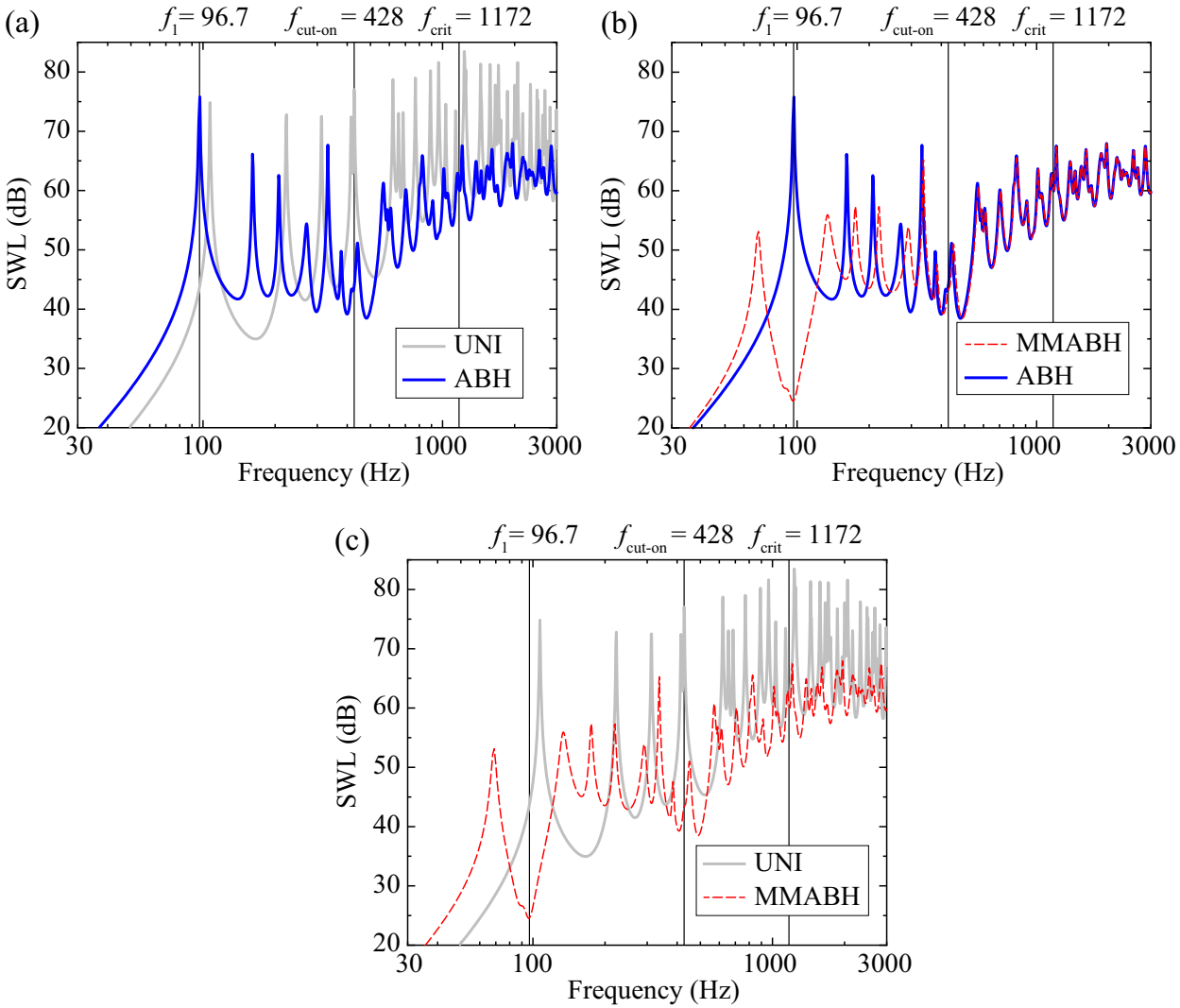

Figure 7: Sound power level (SWL) comparison (a) between the ABH and the reference uniform (UNI) plate, (b) between the MMABH and ABH plate, and (c) between the MMABH and the reference UNI plate.

recirculation problem. As said before, in this work we have favored the NNI because it presents some better behavior at low frequencies [68].

NNI surface plots at $f = \{99, 460, 1206, 2000\}$ Hz have been computed with Eq. (20) and plotted in Fig. 10. It observed that at 99 Hz (first row), the most effective radiating region of the UNI and ABH plates is the plate center. However, the radiation area of the MMABH plate mainly locates in the neighborhood of the force point, and its maximum value is much smaller than those of the other two plates. This is a direct consequence of the bandgap formation by the local resonators. Not only because of their damping effect but mainly because of the group velocity being small, which prevents waves from propagating in the bandgap. As shown in Figs. B.1-B.2, the dispersion curves at the band gap bounds are very flat (their gradient correspond to the group velocity). If we next have a look at the results for 460 Hz (second row), which is much larger than the first modal frequency of the plate but smaller than the critical frequency, it is observed that the active radiating area for the three plates moves to the plate corners. This is consistent with the well-known phenomenon of edge and corner radiation below the critical frequency of a uniform plate, see e.g., [73, 75, 76]. At 1206 Hz (third row), which is bigger than the critical frequency and well-passed the

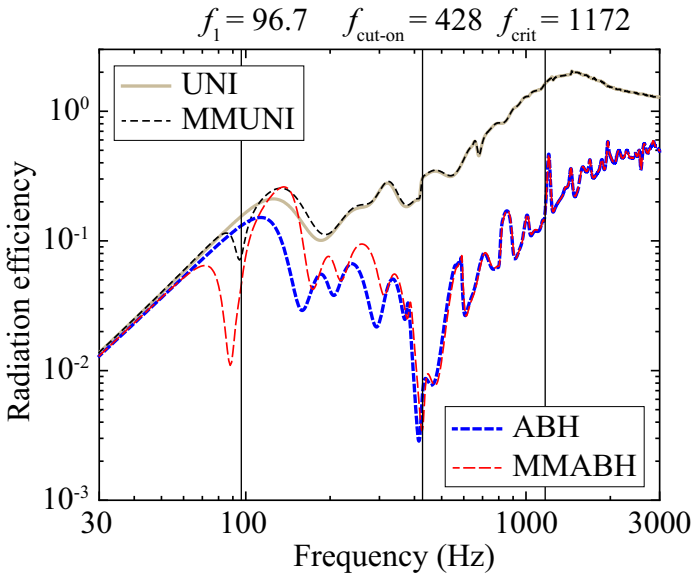

Figure 8: Sound radiation efficiency comparisons among the UNI, MMUNI (UNI plus resonators), ABH, and MMABH (ABH plus resonators) plates.

ABH cut-on frequency, it is clearly seen that the NNI is zero inside the ABH indentation. Therefore the uniform portions of the ABH and MMABH plates are the ones responsible for far-field radiation. The reason for that is the ABH effect, which slows downs supersonic waves entering the indentation and turn them into subsonic. When the frequency is large and well beyond the critical frequency, waves can be still supersonic at the entrance of the ABH, and it takes some distance to diminish their velocity and make them subsonic. This is what occurs at 2000 Hz (fourth row in Fig. 10). One can identify transonic boundaries [22], marked with white dashed circles, where the bending wave propagation velocity transforms from supersonic to subsonic. In this situation the NNI mainly concentrates between the ABH edge and the transonic boundary, because the vibration is more intense there than in the uniform area of the plate and the waves are still supersonic (see Figs. 10b4 and 10c4). In summary, the MMABH can substantially reduce the sound power and far-field sound radiation of plates based on two reasons: i) the bandgap formation and damping effect induced by the local resonators and ii) the ABH effect which traps and slows down waves making them subsonic.

5. Conclusions

In this paper we have investigated the sound radiation properties of the MMABH plate, which is built from an ABH plate with attached local resonators. The resonators are periodically distributed on the plate and have been tuned so that their natural frequency matches the first eigenfrequency of the ABH plate. The MMABH was originally designed to achieve broadband vibration reduction by combining the low-frequency bandgap formation by periodically distributed local resonators, with the ABH effect at mid-high frequencies. In this work, we have observed that the MMABH also provides broadband sound radiation reduction and we have analyzed the reasons why.

A sound radiation model has been built to be able to compute the far-field acoustic pressure radiated by the MMABH, its sound power level and radiation efficiency, and the NNI at its surface. It is clear that the vibration reduction of the MMABH as compared to uniform and ABH plates at low frequencies, and to uniform plates at mid-high frequencies has a profound impact in sound radiation reduction, but there is much more than that. In particular, the differences of radiation efficiency and NNI among plates are very revealing. The radiation efficiency of a finite uniform plate grows from small values at low frequencies to a maximum at the critical frequency and then diminishes to that of an equivalent piston. If we add

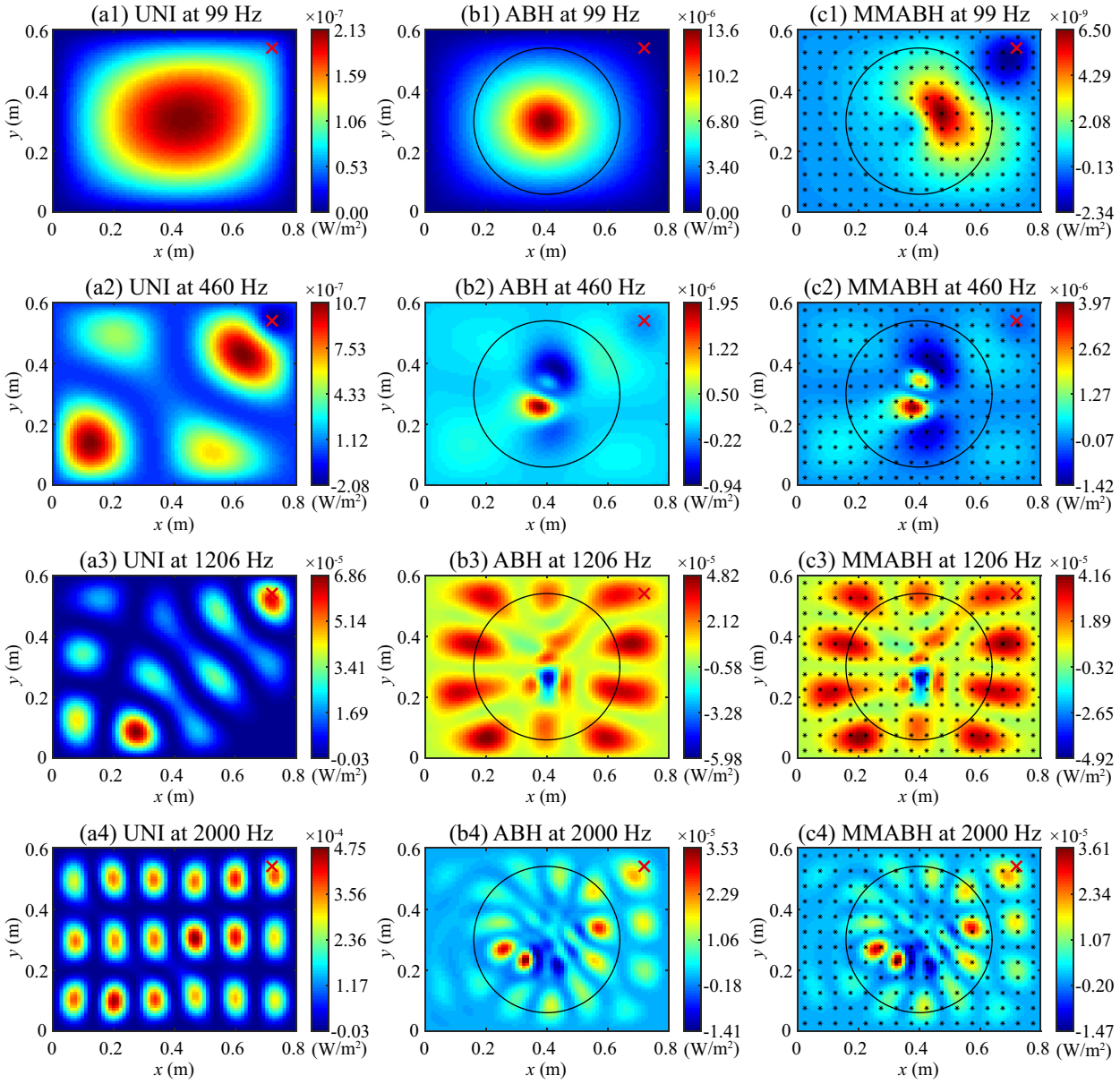

Figure 9: Acoustic intensity distribution on the surface of (a1)-(a4) the UNI plate, (b1)-(b4) the ABH plate, and (c1)-(c4) the MMABH plate, at different frequencies. Different color scales are used to better appreciate the results.

local resonators to the plate, a big drop takes place at the bandgap due to the low-frequency coincidence phenomenon and then the radiation efficiency recovers that of the uniform plate. On the other hand, the inclusion of an ABH indentation strongly decreases the radiation efficiency as one approaches the cut-on frequency. Well-passed the latter, an ABH plate becomes a very poor radiator. The MMABH has the advantage of combining both effects so, in average, one can achieve a low radiation efficiency for the whole frequency range.

Likewise, the analysis of non-negative intensity allows one to understand how the MMABH radiates at the far-field at different frequencies. At the lower ones, within the bandgap, wave propagation is banned and the MMABH only radiates from a small neighborhood of the excitation point. As opposed, both the uniform

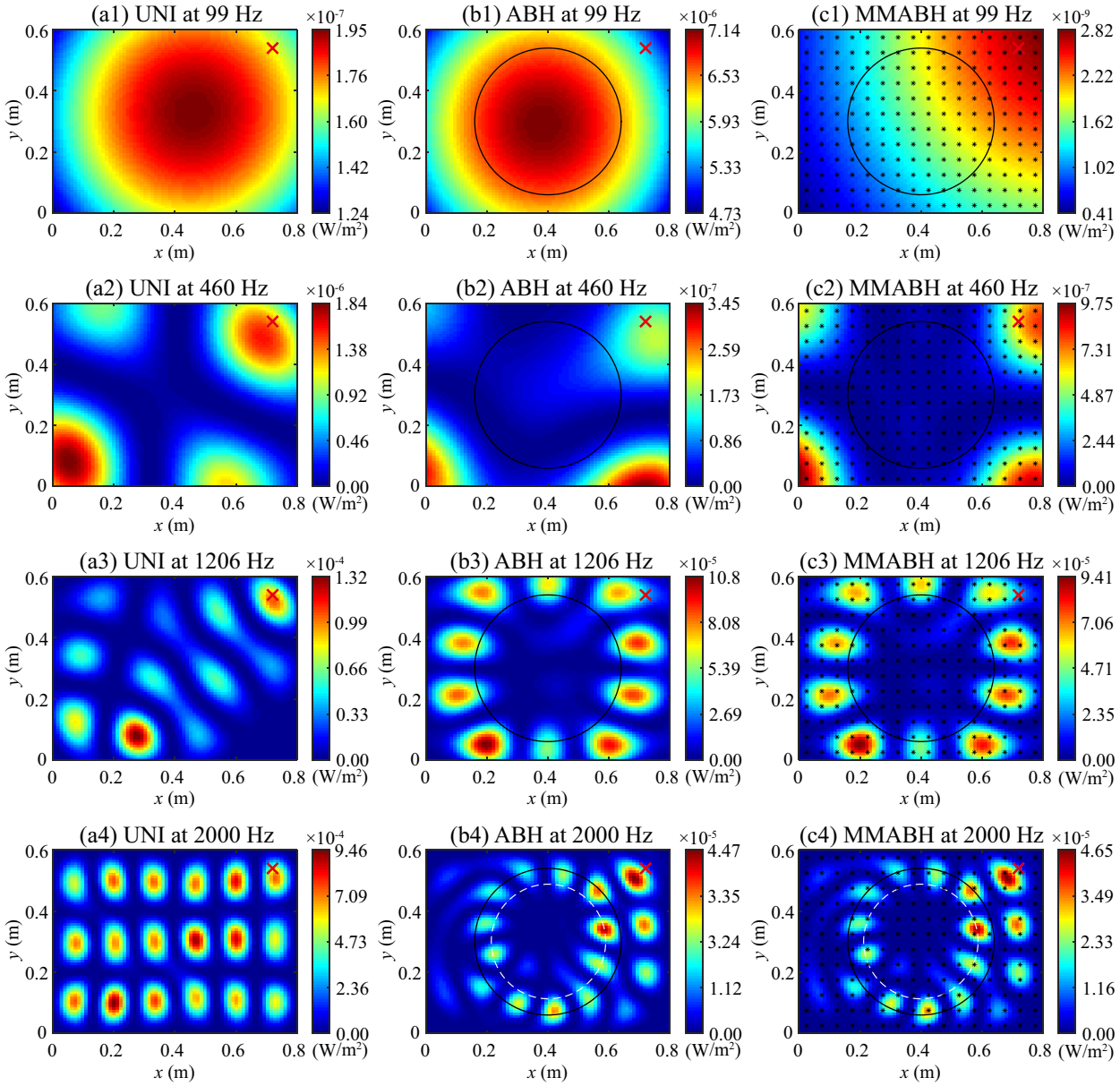

Figure 10: Non-negative intensity distribution on the surface of (a1)-(a4) the UNI plate, (b1)-(b4) ABH plate, and (c1)-(c4) MMABH plate, at different frequencies. The white dashed circles in the last row indicate the transonic boundary. Different color scales are used to better appreciate the results.

and in particular the ABH plate present very high intensity values at their centers. As one approaches the cut-on frequency, corner radiation dominates for the three plates. Close to the critical frequency, which is well passed the cut-on frequency, the ABH and MMABH plates behave identically. The ABH effect is fully operational and waves inside the ABH region are subsonic. Radiation then comes from the outer ABH area. As the frequency augments, it takes some distance for the supersonic waves entering the ABH to slow down and become subsonic, so radiation mainly takes place in the ring region between the transonic boundary and the ABH radius.

To conclude, the MMABH plate looks as a very promising design for both, broadband vibration and sound radiation reduction. In future works, we aim at experimentally testing MMABH-type designs as well

as considering their analogies for other geometries, like cylindrical shells. The potential of MMABH plates for applications like transmission loss between cavities will be also worth investigating. It is to be noted that making ABH plates is not an easy task and including local resonators pose additional difficulties. However, nowadays additive layer manufacturing techniques offer a wide range of possibilities to overcome them.

Acknowledgments

The first author is grateful for the Fundamental Research Funds for the Central Universities, China (Grant No. G2022KY05106). This work is also supported by the National Natural Science Foundation of China (Grant No. 52171323) and the China Postdoctoral Science Foundation (Grant Nos. 2018M631194 and 2020T130533).

Appendix A. Expressions for the mass and stiffness matrices and modal vectors used to compute the MMABH plate surface velocity

For completeness, this appendix provides expressions for the various mass and stiffness matrices, and modal vectors in Section 3.1 (the reader is referred to [53] for details). The mass, $\boldsymbol{M}_p$, and stiffness $\boldsymbol{K}_p$ matrices of the bare ABH plate in Eq. (3) are introduced by developing the expressions for their kinetic energy,

$$\begin{aligned} T_p =& \frac{1}{2}\int_{-\frac{a}{2}}^{\frac{a}{2}}\int_{-\frac{a}{2}}^{\frac{a}{2}} \rho_p h \dot{w}_p^2(x,y,t)\mathrm{d}x\mathrm{d}y = \frac{1}{2}\int_{-\frac{a}{2}}^{\frac{a}{2}}\int_{-\frac{a}{2}}^{\frac{a}{2}} \rho_p h \left[\dot{\boldsymbol{a}}^\top \boldsymbol{\chi}(x,y)\boldsymbol{\chi}^{\mathrm{H}}(x,y)\dot{\boldsymbol{a}}\right]\mathrm{d}x\mathrm{d}y \\ =& \frac{1}{2}\dot{\boldsymbol{a}}^\top \left[\int_{-\frac{a}{2}}^{\frac{a}{2}}\int_{-\frac{a}{2}}^{\frac{a}{2}} \rho_p h \boldsymbol{\chi}(x,y)\boldsymbol{\chi}^{\mathrm{H}}(x,y)\mathrm{d}x\mathrm{d}y\right]\dot{\boldsymbol{a}} \equiv \frac{1}{2}\dot{\boldsymbol{a}}^\top \boldsymbol{M}_p \dot{\boldsymbol{a}}, \end{aligned} \tag{A.1}$$

and potential energy,

$$\begin{aligned} V_p =& \frac{1}{2}\int_{-\frac{a}{2}}^{\frac{a}{2}}\int_{-\frac{a}{2}}^{\frac{a}{2}} D_p \left\{ \left[\frac{\partial^2 w_p}{\partial x^2}(x,y)\right]^2 + \left[\frac{\partial^2 w_p}{\partial y^2}(x,y)\right]^2 + \nu_p \frac{\partial^2 w_p}{\partial x^2}(x,y)\frac{\partial^2 w_p}{\partial y^2}(x,y) \right. \\ & \left. + \nu_p \frac{\partial^2 w_p}{\partial y^2}(x,y)\frac{\partial^2 w_p}{\partial x^2}(x,y) + 2(1-\nu_p)\left[\frac{\partial^2 w_p}{\partial x \partial y}(x,y)\right]^2 \right\}\mathrm{d}x\mathrm{d}y \\ =& \frac{1}{2}\boldsymbol{a}^\top \left\{ \int_{-\frac{a}{2}}^{\frac{a}{2}}\int_{-\frac{a}{2}}^{\frac{a}{2}} D_p \left[\frac{\partial^2 \boldsymbol{\chi}}{\partial x^2}(x,y)\frac{\partial^2 \boldsymbol{\chi}^{\mathrm{H}}}{\partial x^2}(x,y) + \frac{\partial^2 \boldsymbol{\chi}}{\partial y^2}(x,y)\frac{\partial^2 \boldsymbol{\chi}^{\mathrm{H}}}{\partial y^2}(x,y) \right. \right. \\ & + \nu_p \frac{\partial^2 \boldsymbol{\chi}}{\partial x^2}(x,y)\frac{\partial^2 \boldsymbol{\chi}^{\mathrm{H}}}{\partial y^2}(x,y) + \nu_p \frac{\partial^2 \boldsymbol{\chi}}{\partial y^2}(x,y)\frac{\partial^2 \boldsymbol{\chi}^{\mathrm{H}}}{\partial x^2}(x,y) \\ & \left. \left. + 2(1-\nu_p)\frac{\partial^2 \boldsymbol{\chi}}{\partial x \partial y}(x,y)\frac{\partial^2 \boldsymbol{\chi}^{\mathrm{H}}}{\partial y \partial x}(x,y) \right]\mathrm{d}x\mathrm{d}y \right\}\boldsymbol{a} \equiv \frac{1}{2}\boldsymbol{a}^\top \boldsymbol{K}_p \boldsymbol{a}, \end{aligned} \tag{A.2}$$

where $D_p = \frac{E_p h^3}{12(1-\nu_p^2)}$ is the bending stiffness, E_p the Young modulus and ν_p the Poisson ratio.

The vector $\boldsymbol{\varepsilon}$ with time derivative $\dot{\boldsymbol{\varepsilon}}$ in Eqs. (5)-(6) has components $\boldsymbol{\varepsilon} = (\boldsymbol{\varepsilon}_p, \overline{w}_{r1}, \ldots, \overline{w}_{ri}, \ldots, \overline{w}_{rn_x n_y})^\top$. The mass matrix $\overline{\boldsymbol{M}}$ in Eq. (5) is given by,

$$\overline{\boldsymbol{M}} = \begin{bmatrix} \overline{\boldsymbol{M}}_p & \boldsymbol{0} \\ \boldsymbol{0} & \boldsymbol{I} \end{bmatrix}, \tag{A.3}$$

where $\boldsymbol{I}$ stands for the identity matrix of dimensions $n_x n_y \times n_x n_y$. Besides, the stiffness matrix of the i-th resonator $\overline{\boldsymbol{K}}_{ri}$ in Eq. (6) reads,

$$\overline{\boldsymbol{K}}_{ri} = \begin{bmatrix} \overline{\boldsymbol{P}} & 0 \\ 0 & 1 \end{bmatrix}^\top \begin{bmatrix} k_r \boldsymbol{\chi}_i \boldsymbol{\chi}_i^\top & -k_r \boldsymbol{\chi}_i \\ -k_r \boldsymbol{\chi}_i^\top & \omega_r^2 \end{bmatrix} \begin{bmatrix} \overline{\boldsymbol{P}} & 0 \\ 0 & 1 \end{bmatrix}, \tag{A.4}$$

while the total stiffness matrix in the same equation has the expression $\overline{\boldsymbol{K}} = \widetilde{\boldsymbol{P}}^{\top}\widetilde{\boldsymbol{K}}\widetilde{\boldsymbol{P}}$, with

$$\widetilde{\boldsymbol{P}} = \operatorname{diag}\left(\overline{\boldsymbol{P}}, \overbrace{1, 1, 1, \ldots, 1}^{n_x n_y}\right) \tag{A.5}$$

and

$$\widetilde{\boldsymbol{K}} = \begin{bmatrix} \overline{\boldsymbol{K}}_p + k_r \sum_{i=1}^{n_x n_y} \boldsymbol{\chi}_i \boldsymbol{\chi}_i^{\top} & -k_r\boldsymbol{\chi}_1 & -k_r\boldsymbol{\chi}_2 & -k_r\boldsymbol{\chi}_3 & \cdots & -k_r\boldsymbol{\chi}_i & \cdots & -k_r\boldsymbol{\chi}_{n_x n_y} \\ -k_r\boldsymbol{\chi}_1^{\top} & \omega_r^2 & 0 & 0 & \cdots & 0 & \cdots & 0 \\ -k_r\boldsymbol{\chi}_2^{\top} & 0 & \omega_r^2 & 0 & \cdots & 0 & \cdots & 0 \\ -k_r\boldsymbol{\chi}_3^{\top} & 0 & 0 & \omega_r^2 & \cdots & 0 & \cdots & 0 \\ \vdots & \vdots & \vdots & \vdots & \ddots & \vdots & \ddots & \vdots \\ -k_r\boldsymbol{\chi}_i^{\top} & 0 & 0 & 0 & \cdots & \omega_r^2 & \cdots & 0 \\ \vdots & \vdots & \vdots & \vdots & \ddots & \vdots & \ddots & \vdots \\ -k_r\boldsymbol{\chi}_{n_x n_y}^{\top} & 0 & 0 & 0 & \cdots & 0 & \cdots & \omega_r^2 \end{bmatrix}. \tag{A.6}$$

Appendix B. Bandgaps and coincident frequencies of the MMABH plate

To better understand the results reported in Sections 4.4 and 4.5, it is worth analyzing the formation of bandgaps in the MMABH plate and the appearance of coincident frequencies between plate's bending waves and sound propagation in air. To that purpose we consider a unit cell in the MMABH plate and assume it has constant thickness h, where h could vary between h_c and h_{uni}. We will briefly discuss the influence of h in the formation of bandgaps lately in this appendix.

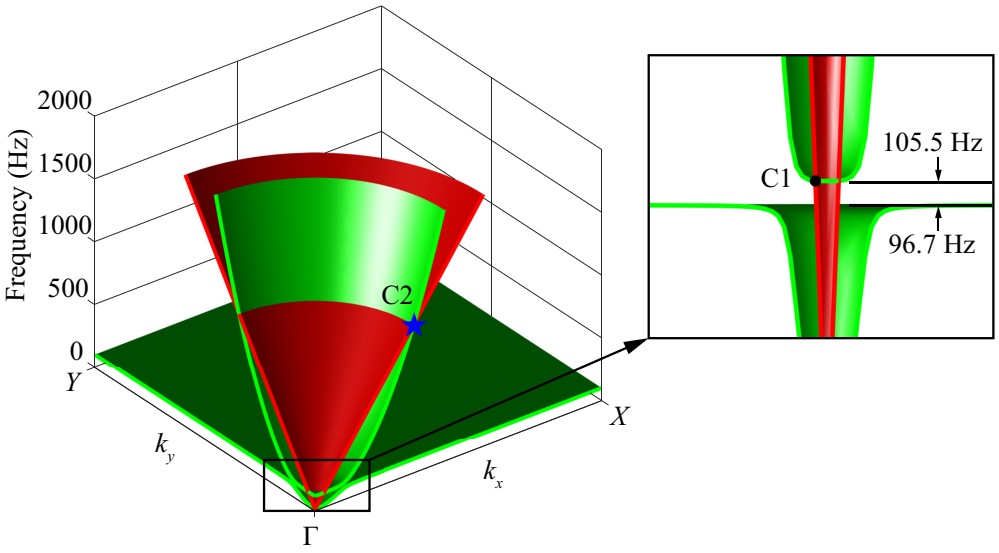

Figure B.1: Dispersion surfaces for an MMABH cell (green) together with that of air (red). The band gap is highlighted in the zoom-in window. The black point and the blue star respectively respectively indicate the low and high frequency coincidence points.

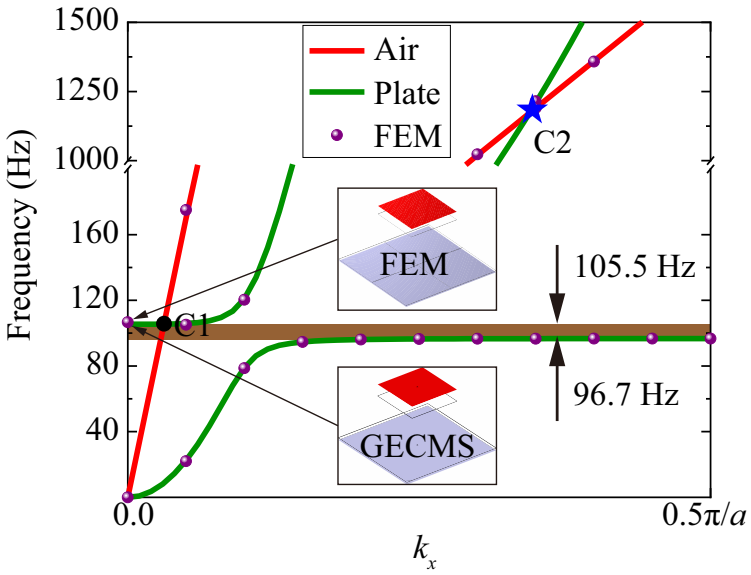

Figure B.2: Dispersion curves computed with the GECMS (solid curves) and with FEM (purple scatters), together with the eigenmodes at the upper bound of the band gap. Note that the ordinate frequency axis is discontinuous in the range $[200, 1000]$ Hz to facilitate inspection.

To determine the dispersion curves and bandgaps in the plate due to the resonators' periodicity, we first need to impose the following periodic conditions on the unit cell boundaries, according to Bloch's theorem,

$$w_p\left(-\frac{a}{2}, y\right) = w_p\left(\frac{a}{2}, y\right) \mathrm{e}^{-\mathrm{i}k_x a}, \;\; w_p\left(x, -\frac{a}{2}\right) = w_p\left(x, \frac{a}{2}\right) \mathrm{e}^{-\mathrm{i}k_y a}, \tag{B.1}$$

$$\frac{\partial w_p}{\partial x}\left(-\frac{a}{2}, y\right) = \frac{\partial w_p}{\partial x}\left(\frac{a}{2}, y\right) \mathrm{e}^{-\mathrm{i}k_x a}, \;\; \frac{\partial w_p}{\partial y}\left(x, -\frac{a}{2}\right) = \frac{\partial w_p}{\partial y}\left(x, \frac{a}{2}\right) \mathrm{e}^{-\mathrm{i}k_y a}, \tag{B.2}$$

$$\frac{\partial^2 w_p}{\partial x^2}\left(-\frac{a}{2}, y\right) = \frac{\partial^2 w_p}{\partial x^2}\left(\frac{a}{2}, y\right) \mathrm{e}^{-\mathrm{i}k_x a}, \;\; \frac{\partial^2 w_p}{\partial y^2}\left(x, -\frac{a}{2}\right) = \frac{\partial^2 w_p}{\partial y^2}\left(x, \frac{a}{2}\right) \mathrm{e}^{-\mathrm{i}k_y a}, \tag{B.3}$$

$$\frac{\partial^3 w_p}{\partial x^3}\left(-\frac{a}{2}, y\right) = -\frac{\partial^3 w_p}{\partial x^3}\left(\frac{a}{2}, y\right) \mathrm{e}^{-\mathrm{i}k_x a}, \;\; \frac{\partial^3 w_p}{\partial y^3}\left(x, -\frac{a}{2}\right) = -\frac{\partial^3 w_p}{\partial y^3}\left(x, \frac{a}{2}\right) \mathrm{e}^{-\mathrm{i}k_y a}. \tag{B.4}$$

Eqs. (B.1)-(B.4) respectively account for periodicity on displacements, rotational angles, bending moments, and shear forces. k_x and k_y stand for the wavenumbers in the x and y directions.

The Gaussian basis functions in Section 3 must next be modified to satisfy conditions Eqs. (B.1) and (B.4), according to the procedure described in [77, 78]. One can then express the plate displacement field $w_p(k_x, k_y, x, y, t)$ in terms of the new basis. Following a procedure analogous to that reported in Section 3, but now taking into account that the mass and stiffness matrices in Appendix A will depend on (k_x, k_y), we can arrive at the following eigenvalue problem for the unit cell with resonator (full details are provided in [53]),

$$\left[\overline{\boldsymbol{K}}(k_x, k_y) - \omega^2 \overline{\boldsymbol{M}}(k_x, k_y)\right] \hat{\boldsymbol{\varepsilon}} = \mathbf{0}. \tag{B.5}$$

Here, the wavenumbers can be restricted to the Brillouin zone, $k_x \times k_y = [-\frac{\pi}{a}, \frac{\pi}{a}] \times [-\frac{\pi}{a}, \frac{\pi}{a}]$, and the dispersion curves and surfaces can be directly obtained from Eq. (B.5).

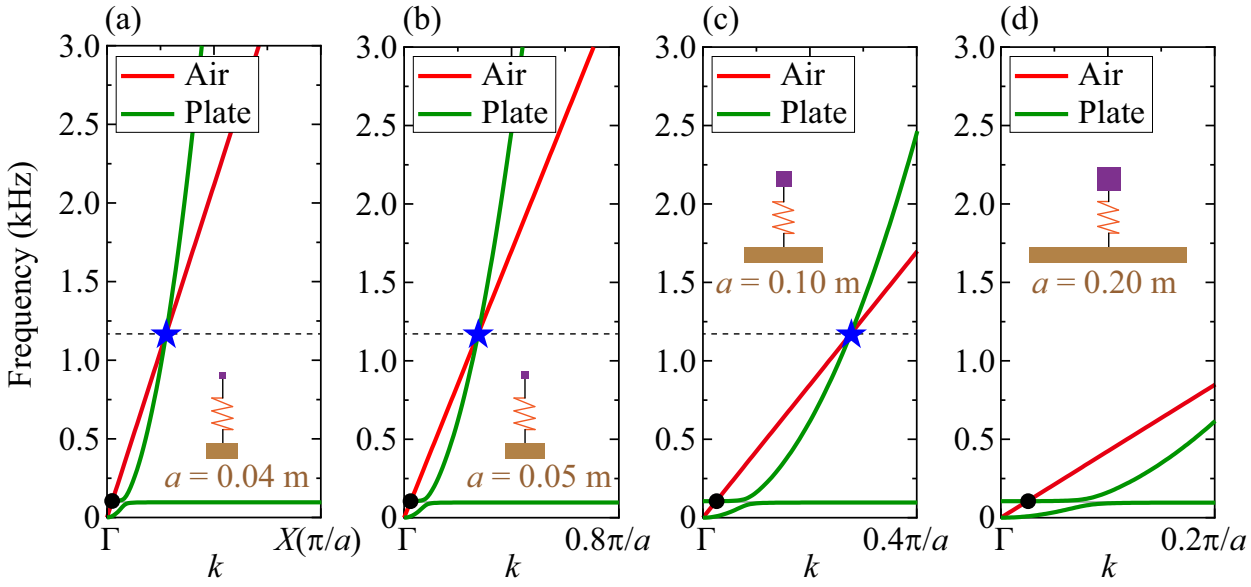

Figure B.3: Dependence of the dispersion curves and coincidence frequencies on the lattice constant a.

In Fig. B.1, we present the first two dispersion surfaces (green color) of the unit cell. As the plate will interact with air, one needs to consider as well the surface, $f = c_0(k_x^2 + k_y^2)^{0.5}/(2\pi)$, where $c_0 = 340$ m/s is the sound speed in air. This has been included in red color in Fig. B.1. On the one hand, it can be observed from the figure that a band gap appears between 96.7 Hz and 105.5 Hz (see the zoom-in window), which is caused by the periodic distribution of resonators. On the other hand, we note that the red (air) and second green (plate) surfaces interact twice in the figure (see Points C1 and C2), at frequencies $f_{C1} = 105.6$ Hz and $f_{C2} = 1172$ Hz. It is well-known that the slope of the line connecting the origin and an arbitrary

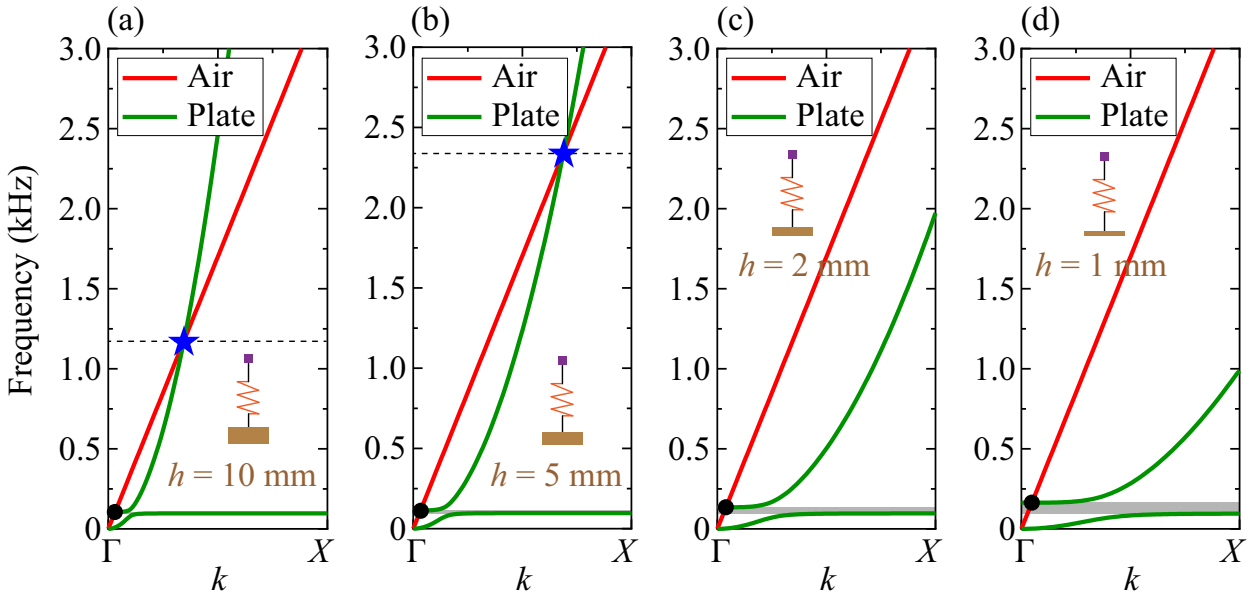

Figure B.4: Dependence of the dispersion curves and coincidence frequencies on the plate thickness h.

point on the dispersion surface represents the phase velocity of the wave, which means that at Points C1 and C2 the plate bending wave velocity coincides with the speed of sound. f_{C1} and f_{C2} are known as the coincidence frequencies. The second one, f_{C2}, simply corresponds to the classical critical frequency, $f_{\text{crit}} = \frac{c_0^2}{2\pi h_{\text{uni}}}\left[\frac{12\rho_p(1-\nu_p^2)}{E_p}\right]^{1/2} = 1172$ Hz, which has nothing to do with metamaterials. However, f_{C1} is a direct consequence of the presence of the resonators as it appears in the vicinity of the upper bound of the bandgap. This phenomenon is known as low-frequency coincidence. The influence of the coincidence frequencies on sound radiated by the MMABH plate is discussed in Section 4.4 of the main text.

The above results obtained from the GECMS have been validated against FEM simulations using the *Shell-Acoustic Pressure* module from the commercial software Comsol Multiphysics. A periodic thin air layer of thickness $h_a = 0.05$ m was coupled to the unit cell in the FEM model. In Fig. B.2, we have represented the dispersion curves within $[0, 0.5\pi/a]$ (note that the ordinate frequency axis is discontinuous between 200 Hz and 1000 Hz to ease the inspection of the results). It is apparent from the figure that the dispersion curves obtained from both methods, GECMS and FEM, are almost identical. The eigenmodes at the upper bound of the bandgap (shaded in brown) are also plotted in the figure for the GEMCS and FEM. Once more, no perceptible differences are found.

It is next worthwhile studying how the number of resonators on the MMABH may affect the bandgap formation and coincidence frequencies. The influence of the resonators' distribution on the MMABH vibration was already analyzed in [53], so we will focus hereafter on its effect on sound radiation. We can increase/decrease the number of resonators but keep the total mass constant by redistributing ΔM among them. Four cases are considered corresponding to $n_x \times n_y = \{20 \times 15, 16 \times 12, 8 \times 6, 4 \times 3\} = \{300, 192, 48, 12\}$ which imply resonators with masses $\Delta M_r = \{0.0235, 0.0368, 0.1470, 0.5881\}$ kg, stiffness $k_r = \{8684, 13569, 54276, 21710\}$ N/m and plate lattice constants $a = \{0.04, 0.05, 0.1, 0.2\}$ m, respectively. In Fig. B.3 the dispersion curves in the $\Gamma - X$ direction are plotted for the four cases, together with the bandgaps and coincidence points. It is observed that the bandgap is almost unaffected by lattice constant variations. Neither the low and high coincidence frequencies get modified as well. This means that the metamaterial properties are barely affected by the lattice constant as long as the total mass is kept constant. In real situations, however, a plate will always have finite dimensions and periodicity will deteriorate for large lattice constant values.

Given that the thickness h of the ABH in the MMABH plate changes from $h_{\text{uni}} = 10$ mm to $h_c = 1$ mm (see Table 1), it is also interesting to analyze the effect that h has on the bandgaps and coincidence frequencies. In Fig. B.4 we plot the same type of results shown in Fig. B.3, but now for varying thickness $h = \{10, 5, 2, 1\}$ mm and constant lattice value $a = 0.05$ m. It is clearly observed that the width of the bandgap augments for decreasing thickness. The lower bound of the bandgap, $f_{\text{low}} = \{96.698, 96.684, 96.448, 95.090\}$ Hz, exhibits little variation but the upper one changes substantially, $f_{\text{up}} = \{105.49, 113.47, 134.72, 163.70\}$ Hz. One could then expect that the ABH could broaden the bandgap to some extent and help reducing low frequency vibrations. Moreover, we also observe in the figure that as the thickness decreases the local slope of the dispersion curves diminishes, which moves the coincidence frequencies to higher values. The low-frequency coincidence slightly increases its value because it moves with the upper bound of the bandgap. As regards the classical critical frequency, it grows with decreasing thickness because the plate flexural wave velocity diminishes with h. At the critical frequency the radiation efficiency of a plate achieves its maximum and in some cases, this adverse effect may overcome the benefits brought by the resonators [79, 80]. Therefore, the latter have to be carefully designed. The influence of h on the MMABH radiation efficiency is discussed in Section 4.4 of the main text.

References

[1] V. V. Krylov, A new type of vibration damper based on flexural wave propagation in laminated wedges of power-law profile, J. Acoust. Soc. Am. 110 (2001) 2654–2654.

[2] M. A. Mironov, Propagation of a flexural wave in a plate whose thickness decreases smoothly to zero in a finite interval, Sov. Phys. Acoust. 34 (1988) 318–319.

[3] V. V. Krylov, F. Tilman, Acoustic black holes for flexural waves as effective vibration dampers, J. Sound Vib. 274 (2004) 605–619.

[4] J. Deng, L. Zheng, P. Zeng, Y. Zuo, O. Guasch, Passive constrained viscoelastic layers to improve the efficiency of truncated acoustic black holes in beams, Mech. Syst. Signal Process. 118 (2019) 461–476.
[5] J. Y. Lee, W. Jeon, Vibration damping using a spiral acoustic black hole, J. Acoust. Soc. Am. 141 (2017) 1437–1445.
[6] S. Park, M. Kim, W. Jeon, Experimental validation of vibration damping using an archimedean spiral acoustic black hole, J. Sound Vib. 459 (2019) 114838.
[7] V. B. Georgiev, J. Cuenca, F. Gautier, L. Simon, V. V. Krylov, Damping of structural vibrations in beams and elliptical plates using the acoustic black hole effect, J. Sound Vib. 330 (2011) 2497–2508.
[8] D. J. O'Boy, V. V. Krylov, Damping of flexural vibrations in circular plates with tapered central holes, J. Sound Vib. 330 (2011) 2220–2236.
[9] O. Aklouche, A. Pelat, S. Maugeais, F. Gautier, Scattering of flexural waves by a pit of quadratic profile inserted in an infinite thin plate, J. Sound Vib. 375 (2016) 38–52.
[10] D. J. O'Boy, V. V. Krylov, Vibration of a rectangular plate with a central power-law profiled groove by the Rayleigh–Ritz method, Appl. Acoust. 104 (2016) 24–32.
[11] T. Zhou, L. Tang, H. Ji, J. Qiu, L. Cheng, Dynamic and static properties of double-layered compound acoustic black hole structures, Int. J. Appl. Mech. 9 (2017) 1750074.
[12] L. Tang, L. Cheng, Impaired sound radiation in plates with periodic tunneled Acoustic Black Holes, Mech. Syst. Signal Process. 135 (2020) 106410.
[13] J. Deng, O. Guasch, L. Zheng, Ring-shaped acoustic black holes for broadband vibration isolation in plates, J. Sound Vib. 458 (2019) 109–122.
[14] J. Deng, O. Guasch, L. Zheng, A semi-analytical method for characterizing vibrations in circular beams with embedded acoustic black holes, J. Sound Vib. 476 (2020) 115307.
[15] J. Deng, O. Guasch, L. Maxit, L. Zheng, Reduction of Bloch-Floquet bending waves via annular acoustic black holes in periodically supported cylindrical shell structures, Appl. Acoust. 169 (2020) 107424.
[16] J. Deng, O. Guasch, L. Maxit, L. Zheng, Vibration of cylindrical shells with embedded annular acoustic black holes using the Rayleigh-Ritz method with Gaussian basis functions, Mech. Syst. Signal Process. 150 (2021) 107225.
[17] A. Pelat, F. Gautier, S. C. Conlon, F. Semperlotti, The acoustic black hole: A review of theory and applications, J. Sound Vib. 476 (2020) 115316.
[18] E. P. Bowyer, V. V. Krylov, Experimental study of sound radiation by plates containing circular indentations of power-law profile, Appl. Acoust. 88 (2015) 30–37.
[19] S. Conlon, J. Fahnline, F. Semperlotti, Numerical analysis of the vibroacoustic properties of plates with embedded grids of acoustic black holes, J. Acoust. Soc. Am. 137 (2015) 447–457.
[20] X. Li, Q. Ding, Sound radiation of a beam with a wedge-shaped edge embedding acoustic black hole feature, J. Sound Vib. 439 (2019) 287–299.
[21] X. Wang, H. Ji, J. Qiu, L. Cheng, Wavenumber domain analyses of vibro-acoustic decoupling and noise attenuation in a plate-cavity system enclosed by an acoustic black hole plate, J. Acoust. Soc. Am. 146 (2019) 72–84.
[22] L. Ma, L. Cheng, Sound radiation and transonic boundaries of a plate with an acoustic black hole, J. Acoust. Soc. Am. 145 (2019) 164–172.
[23] L. Ma, L. Cheng, Topological optimization of damping layout for minimized sound radiation of an acoustic black hole plate, J. Sound Vib. 458 (2019) 349–364.
[24] L. Ma, L. Cheng, Numerical and experimental benchmark solutions on vibration and sound radiation of an Acoustic Black Hole plate, Appl. Acoust. 163 (2020) 107223.
[25] L. Tang, N. Gao, J. Xu, K. Chen, L. Cheng, A light-weight periodic plate with embedded acoustic black holes and bandgaps for broadband sound radiation reduction, J. Acoust. Soc. Am. 150 (2021) 3532–3543.
[26] H. Ji, X. Wang, J. Qiu, L. Cheng, Y. Wu, C. Zhang, Noise reduction inside a cavity coupled to a flexible plate with embedded 2-D acoustic black holes, J. Sound Vib. 455 (2019) 324–338.
[27] J. Deng, L. Zheng, Noise reduction via three types of acoustic black holes, Mech. Syst. Signal Process. 165 (2022) 108323.
[28] P. A. Feurtado, S. C. Conlon, Transmission loss of plates with embedded acoustic black holes, J. Acoust. Soc. Am. 142 (2017) 1390–1398.
[29] X. Du, D. Huang, Q. Fu, J. Zhang, Effects of acoustic black hole parameters and damping layer on sound insulation performance of abh circular plate, Appl. Sci. 9 (2019) 5366.
[30] J. Deng, O. Guasch, L. Maxit, L. Zheng, Transmission loss of plates with multiple embedded acoustic black holes using statistical modal energy distribution analysis, Mech. Syst. Signal Process. 150 (2021) 107262.
[31] V. Denis, A. Pelat, C. Touzé, F. Gautier, Improvement of the acoustic black hole effect by using energy transfer due to geometric nonlinearity, Int. J. Non Linear Mech. 94 (2017) 134–145.
[32] V. E. Gusev, C. Ni, A. Lomonosov, Z. Shen, Propagation of flexural waves in inhomogeneous plates exhibiting hysteretic nonlinearity: Nonlinear acoustic black holes, Ultrasonics 61 (2015) 126–135.
[33] H. Li, C. Touzé, A. Pelat, F. Gautier, X. Kong, A vibro-impact acoustic black hole for passive damping of flexural beam vibrations, J. Sound Vib. 450 (2019) 28–46.
[34] H. Li, C. Touz, F. Gautier, A. Pelat, Linear and nonlinear dynamics of a plate with acoustic black hole, geometric and contact nonlinearity for vibration mitigation, J. Sound Vib. 508 (2021) 116206.
[35] H. Li, M. Scail-Graud, A. Pelat, F. Gautier, C. Touz, Experimental evidence of energy transfer and vibration mitigation in a vibro-impact acoustic black hole, Appl. Acoust. 182 (2021) 108168.
[36] W. Huang, C. Tao, H. Ji, J. Qiu, Enhancement of wave energy dissipation in two-dimensional acoustic black hole by simultaneous optimization of profile and damping layer, J. Sound Vib. 491 (2021) 115764.
[37] L. Tang, L. Cheng, Enhanced acoustic black hole effect in beams with a modified thickness profile and extended platform,

J. Sound Vib. 391 (2017) 116–126.
[38] M. R. Shepherd, P. A. Feurtado, S. C. Conlon, Multi-objective optimization of acoustic black hole vibration absorbers, J. Acoust. Soc. Am. 140 (2016) EL227–EL230.
[39] M.-X. He, Q. Ding, Data-driven optimization of the periodic beam with multiple acoustic black holes, J. Sound Vib. 493 (2021) 115816.
[40] L. Tang, L. Cheng, K. Chen, Complete sub-wavelength flexural wave band gaps in plates with periodic acoustic black holes, J. Sound Vib. 502 (2021) 116102.
[41] S. Nair, M. Jokar, F. Semperlotti, Nonlocal acoustic black hole metastructures: Achieving broadband and low frequency passive vibration attenuation, Mech. Syst. Signal Process. 169 (2022) 108716.
[42] Z. Liu, X. Zhang, Y. Mao, Y. Y. Zhu, Z. Yang, C. T. Chan, P. Sheng, Locally resonant sonic materials, Science 289 (2000) 1734–1736.
[43] D. Roca, J. Cante, O. Lloberas-Valls, T. Pmies, J. Oliver, Multiresonant layered acoustic metamaterial (mlam) solution for broadband low-frequency noise attenuation through double-peak sound transmission loss response, Extreme Mech. Lett. 47 (2021) 101368.
[44] C. Mei, L. Li, H. Tang, X. Han, X. Wang, Y. Hu, Broadening band gaps of shear horizontal waves of metamaterials via graded hierarchical architectures, Compos. Struct. 271 (2021) 114118.
[45] C. Liu, J. Wu, Z. Yang, F. Ma, Ultra-broadband acoustic absorption of a thin microperforated panel metamaterial with multi-order resonance, Comput. Struct. 246 (2020) 112366.
[46] P. Gao, A. Climente, J. Sánchez-Dehesa, L. Wu, Single-phase metamaterial plates for broadband vibration suppression at low frequencies, J. Sound Vib. 444 (2019) 108–126.
[47] W. Tian, T. Zhao, Z. Yang, Theoretical modelling and design of metamaterial stiffened plate for vibration suppression and supersonic flutter, Compos. Struct. 282 (2022) 115010.
[48] F. Pires, C. Claeys, E. Deckers, W. Desmet, The impact of resonant additions footprint on the stop band behavior of 1D locally resonant metamaterial realizations, J. Sound Vib. 491 (2021) 115705.
[49] Z. Xiao, P. Gao, D. Wang, X. He, L. Wu, Ventilated metamaterials for broadband sound insulation and tunable transmission at low frequency, Extreme Mech. Lett. 46 (2021) 101348.
[50] Z. Liu, R. Rumpler, L. Feng, Broadband locally resonant metamaterial sandwich plate for improved noise insulation in the coincidence region, Compos. Struct. 200 (2018) 165–172.
[51] A. Climente, P. Gao, L. Wu, J. Snchez-Dehesa, Scattering of flexural waves from an N-beam resonator in a thin plate, J. Acoust. Soc. Am. 142 (2017) 3205.
[52] P. Gao, A. Climente, J. Sánchez-Dehesa, L. Wu, Theoretical study of platonic crystals with periodically structured N-beam resonators, J. Appl. Phys. 123 (2018) 091707.
[53] J. Deng, O. Guasch, L. Maxit, N. Gao, A metamaterial consisting of an acoustic black hole plate with local resonators for broadband vibration reduction, J. Sound Vib. 526 (2022) 116803.
[54] J. Deng, L. Zheng, O. Guasch, H. Wu, P. Zeng, Y. Zuo, Gaussian expansion for the vibration analysis of plates with multiple acoustic black holes indentations, Mech. Syst. Signal Process. 131 (2019) 317–334.
[55] A. F. Russillo, G. Failla, A novel reduced-order dynamic-stiffness formulation for locally resonant metamaterial plates, Compos. Struct. 280 (2022) 114811.
[56] J. Deng, Y. Xu, O. Guasch, N. Gao, L. Tang, Nullspace technique for imposing constraints in the Rayleigh–Ritz method, J. Sound Vib. 527 (2022) 116812.
[57] N. Chandra, S. Raja, K. Nagendra Gopal, Vibro-acoustic response and sound transmission loss analysis of functionally graded plates, J. Sound Vib. 333 (2014) 5786–5802.
[58] N. Chandra, K. Nagendra Gopal, S. Raja, Vibro-acoustic response of sandwich plates with functionally graded core, Acta Mech. 228 (2017) 2775–2789.
[59] J. Deng, N. Gao, L. Tang, H. Hou, K. Chen, L. Zheng, Vibroacoustic mitigation for a cylindrical shell coupling with an acoustic black hole plate using Gaussian expansion component mode synthesis, Compos. Struct. 298 (2022) 116002.
[60] J. Deng, N. Gao, Broadband vibroacoustic reduction for a circular beam coupled with a curved acoustic black hole via nullspace method, Int. J. Mech. Sci. 233 (2022) 107641.
[61] J. Deng, O. Guasch, L. Maxit, L. Zheng, Annular acoustic black holes to reduce sound radiation from cylindrical shells, Mech. Syst. Signal Process. 158 (2021) 107722.
[62] D. Liu, H. Peters, S. Marburg, N. Kessissoglou, Surface contributions to scattered sound power using non-negative intensity, J. Acoust. Soc. Am. 140 (2016) 1206–1217.
[63] D. R. Wilkes, H. Peters, P. Croaker, S. Marburg, A. J. Duncan, N. Kessissoglou, Non-negative intensity for coupled fluidstructure interaction problems using the fast multipole method, J. Acoust. Soc. Am. 141 (2017) 4278–4288.
[64] D. Liu, Z. Havrnek, S. Marburg, H. Peters, N. Kessissoglou, Non-negative intensity and back-calculated non-negative intensity for analysis of directional structure-borne sound, J. Acoust. Soc. Am. 142 (2017) 117–123.
[65] D. Liu, S. Marburg, C. Geweth, N. Kessissoglou, Non-negative intensity for structures with inhomogeneous damping, J. Theor. Comp. Acout. 27 (2019) 1850050.
[66] E. G. Williams, Supersonic acoustic intensity, J. Acoust. Soc. Am. 97 (1995) 121–127.
[67] E. Fernandez-Grande, F. Jacobsen, Q. Leclere, Direct formulation of the supersonic acoustic intensity in space domain, J. Acoust. Soc. Am. 131 (2012) 186–193.
[68] D. Liu, H. Peters, S. Marburg, N. Kessissoglou, Supersonic intensity and non-negative intensity for prediction of radiated sound, J. Acoust. Soc. Am. 139 (2016) 2797–2806.
[69] M. R. Bai, M. Tsao, Estimation of sound power of baffled planar sources using radiation matrices, J. Acoust. Soc. Am. 112 (2002) 876–883.

[70] A. P. Berkhoff, Sensor scheme design for active structural acoustic control, J. Acoust. Soc. Am. 108 (2000) 1037–1045.
[71] F. J. Fahy, P. Gardonio, Sound and structural vibration: radiation, transmission and response, Elsevier, 2007.
[72] E. G. Williams, Supersonic acoustic intensity on planar sources, J. Acoust. Soc. Am. 104 (1998) 2845–2850.
[73] S. Marburg, E. Lsche, H. Peters, N. Kessissoglou, Surface contributions to radiated sound power, J. Acoust. Soc. Am. 133 (2013) 3700–3705.
[74] L. Van Belle, C. Claeys, E. Deckers, W. Desmet, The impact of damping on the sound transmission loss of locally resonant metamaterial plates, J. Sound Vib. 461 (2019) 114909.
[75] C. Deffayet, P. A. Nelson, Active control of low-frequency harmonic sound radiated by a finite panel, J. Acoust. Soc. Am. 84 (1988) 2192–2199.
[76] G. Maidanik, Response of ribbed panels to reverberant acoustic fields, J. Acoust. Soc. Am. 34 (1962) 809–826.
[77] J. Deng, O. Guasch, L. Zheng, Reconstructed Gaussian basis to characterize flexural wave collimation in plates with periodic arrays of annular acoustic black holes, Int. J. Mech. Sci. 194 (2021) 106179.
[78] J. Deng, L. Zheng, N. Gao, Broad band gaps for flexural wave manipulation in plates with embedded periodic strip acoustic black holes, Int. J. Solids Struct. 224 (2021) 111043.
[79] J. Jung, H.-G. Kim, S. Goo, K.-J. Chang, S. Wang, Realisation of a locally resonant metamaterial on the automobile panel structure to reduce noise radiation, Mech. Syst. Signal Process. 122 (2019) 206–231.
[80] Q. Qin, M. Sheng, Z. Guo, Low-frequency vibration and radiation performance of a locally resonant plate attached with periodic multiple resonators, Appl. Sci. 10 (2020) 2843.